remote sensing

MDPI

Review

Review of Assimilating Spaceborne Global Navigation Satellite System Remote Sensing Data for Tropical Cyclone Forecasting

Weihua Bai [1,2,3,4,†], Guanyi Wang [1,2,3,4,†], Feixiong Huang [1,2,4,*], Yueqiang Sun [1,2,3,4], Qifei Du [1,2,4], Junming Xia [1,2,4], Xianyi Wang [1,2,4], Xiangguang Meng [1,2,4], Peng Hu [1,2,4], Cong Yin [1,2,4], Guangyuan Tan [1,2,4] and Ruhan Wu [1,2,4]

1 National Space Science Center, Chinese Academy of Sciences (NSSC/CAS), Beijing 100190, China; baiweihua@nssc.ac.cn (W.B.); wangguanyi22@mails.ucas.ac.cn (G.W.); syq@nssc.ac.cn (Y.S.); dqf@nssc.ac.cn (Q.D.); xiajunming@nssc.ac.cn (J.X.); wxy@nssc.ac.cn (X.W.); xgmeng@nssc.ac.cn (X.M.); hupeng@nssc.ac.cn (P.H.); yincong@nssc.ac.cn (C.Y.); tanguangyuan16@mails.ucas.ac.cn (G.T.); wuruhan@nssc.ac.cn (R.W.)
2 Beijing Key Laboratory of Space Environment Exploration, Beijing 100190, China
3 School of Astronomy and Space Science, University of Chinese Academy of Sciences, Beijing 100049, China
4 Joint Laboratory on Occultations for Atmosphere and Climate (JLOAC), National Space Science Center, Chinese Academy of Sciences and University of Graz, Beijing 100190, China
* Correspondence: huangfeixiong@nssc.ac.cn
† These authors contributed equally to this work.

Abstract: Global Navigation Satellite System (GNSS) Radio Occultation (RO) and GNSS Reflectometry (GNSS-R) are the two major spaceborne GNSS remote sensing (GNSS-RS) techniques, providing observations of atmospheric profiles and the Earth's surface. With the rapid development of GNSS-RS techniques and spaceborne missions, many experiments and studies were conducted to assimilate those observational data into numerical weather-prediction models for tropical cyclone (TC) forecasts. GNSS RO data, known for its high precision and all-weather observation capability, is particularly effective in forecasting mid-to-upper atmospheric levels. GNSS-R, on the other hand, plays a significant role in improving TC track and intensity predictions by observing ocean surface winds under high precipitation in the inner core of TCs. Different methods were developed to assimilate these remote sensing data. This review summarizes the results of assimilation studies using GNSS-RS data for TC forecasting. It concludes that assimilating GNSS RO data mainly enhances the prediction of precipitation and humidity, while assimilating GNSS-R data improves forecasts of the TC track and intensity. In the future, it is promising to combine GNSS RO and GNSS-R data for joint retrieval and assimilation, exploring better effects for TC forecasting.

Keywords: GNSS RO; GNSS-R; tropical cyclone; forecast

check for updates

Academic Editor: Yuriy Kuleshov

Received: 1 November 2024
Revised: 28 November 2024
Accepted: 2 December 2024
Published: 1 January 2025

Citation: Bai, W.; Wang, G.; Huang, F.; Sun, Y.; Du, Q.; Xia, J.; Wang, X.; Meng, X.; Hu, P.; Yin, C.; et al. Review of Assimilating Spaceborne Global Navigation Satellite System Remote Sensing Data for Tropical Cyclone Forecasting. *Remote Sens.* **2025**, *17*, 118. https://doi.org/10.3390/rs17010118

Copyright: © 2025 by the authors. Licensee MDPI, Basel, Switzerland. This article is an open access article distributed under the terms and conditions of the Creative Commons Attribution (CC BY) license (https://creativecommons.org/licenses/by/4.0/).

1. Introduction

Tropical cyclones (TCs) are deep convective systems often accompanied by destructive weather conditions, such as strong winds, heavy rainfall, and thunderstorms. Their formation and development are influenced by various meteorological factors. TC forecasting mainly relies on weather-prediction models, numerically or using artificial intelligence [1,2]. In a recent study, the forecast accuracy results of TCs using various operational numerical weather prediction (NWP) models are compared. There are three verification criteria: hit, false alarm, and miss [3]. A hit is a successful prediction where the location is near 5° of the targeted TC and the time is within 24 h of the targeted TC. A miss is the opposite of a hit. A

false alarm means that a TC forecast is made, but the time and track are incorrect. They investigated the prediction results of TCs using global NWP models, including the Global Environmental Multiscale Model of Environment and Climate Change Canada (CMC), the European Centre for Medium-Range Weather Forecasts global model (ECMWF), the Environmental Prediction Global Forecast System (GFS) of the American National Centers, and the Met Office Global Model (UKMET) [4]. Most predictions fell into the false alarm and miss categories as shown in Figure 1.

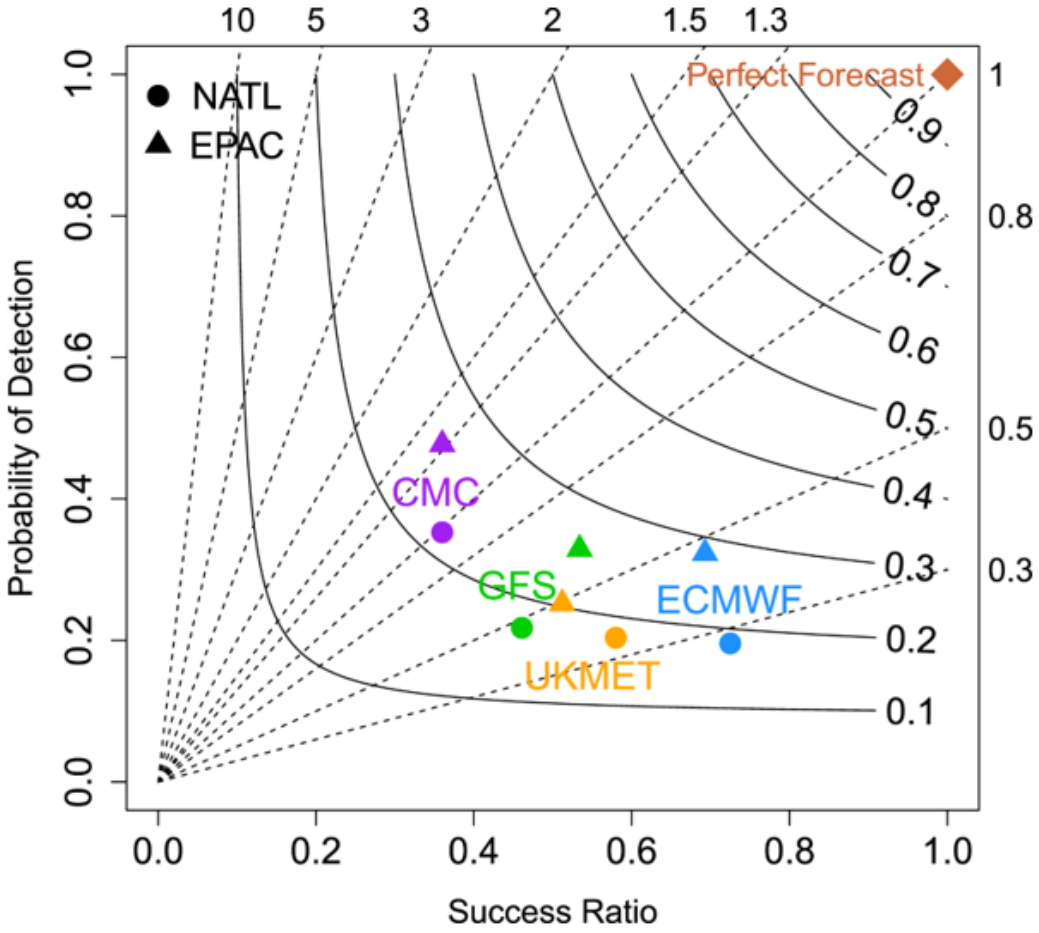

Figure 1. Mean forecast performance for each model over the North Atlantic (circle) and eastern North Pacific (triangle) basins [5].

The accurate forecast of a TC relies on a forecast model and an accurate initial guess of all atmospheric parameters, i.e., the model state. The initial guess is usually generated by a series, combining the forecast of the model and actual observations called data assimilation. The data assimilation utilizes actual observations with errors from different platforms and techniques to correct the model forecast and produce the best estimations of the model state. Therefore, observations with a large quantity and high accuracy are crucial to weather forecasts. In the mesoscale and global weather forecast, over 90% of observations are from satellite platforms. Satellites can provide a large number of observations on a global scale especially over the ocean using different remote sensing techniques. However, for the observations of TCs, many optical and microwave remote sensing technique observations cannot penetrate the cloud and heavy rains near the center of TCs, limiting the forecasting of the TC track and intensity.

GNSS (Global Navigation Satellite System) remote sensing (GNSS-RS) is a new technique that has been developed in recent decades. Currently acknowledged GNSS systems include US GPS, European GALILEO, Russian GLONASS, and Chinese BeiDou, which

provide real-time, all-weather, anytime, anywhere, and high-precision observations by transmitting L band signals continuously. They have been broadly applied for positioning, navigation, and timing [6]. Based on the application and propagation of GNSS signals, there are mainly two branches of GNSS-RS: GNSS Radio Occultation (RO) and GNSS Reflectometry (GNSS-R). The former uses the GNSS signals refraction when they pass through the atmosphere, while the latter utilizes the reflection of the signals on the Earth's surface [7].

GNSS RO observations have many advantages, including global coverage, high accuracy, high vertical resolution, and insensitivity to clouds and precipitation, allowing for all-weather observations. For the troposphere, the departure of temperature, pressure, and potential temperature measured using RO is 0.7 K, 0.15%, and 1.4 K, and also the vertical resolution can reach 1.5 km [8]. With the development of background information, the departure becomes smaller as it gets closer to the lower troposphere [9]. For the troposphere and near the surface, the vertical resolution can reach 0.2 km or even 0.1 km [10]. As long as there are enough satellites equipped with RO receivers, RO data can achieve denser global coverage, especially in areas where conventional observation methods are lacking, such as the poles and oceans. Additionally, RO is a self-calibrating remote sensing technique and can be regarded as a calibration standard for other observation methods [11,12]. Self-calibrating measures the change in the signal's properties, such as the phase delay. Therefore, RO data are traceable to GNSS atomic clocks and have a low bias. Also, it eliminates the need for instruments and is not affected by aging or environmental changes of observing instruments. That leads to high long-term stability over decades. By comparing the outputs from other sensors (such as radiometers or hyperspectral sounders) with RO, biases and drifts can be corrected. Because there is no need for external or repeated recalibrations, the RO technique is more efficient and cost-effective.

Spaceborne GNSS-R remote sensing also provides global coverage and all-weather monitoring. Its low cost and rapid revisit are additional advantages, making it an effective complement to traditional altimetric and scatterometric ocean observations [13]. GNSS-R measurements operate in the L-band (1–2 GHz), where the lower frequency results in less rainfall attenuation, increasing the likelihood of observing the inner core of TCs. Additionally, the smaller size, weight, and power consumption of GNSS-R measurements make them less costly to manufacture and use [14]. The small satellite constellation offers better temporal and spatial sampling than conventional techniques. The real-time and near real-time operational applications require high spatial and temporal sampling rates, such as operational NWP models, and TC monitoring.

With great advantages, GNSS-RS data from different satellite missions have been assimilated into different NWP models, where the impact on TC forecasts has been presented by a number of studies.

This paper will give a comprehensive review of the method and impacts of assimilating GNSS remote sensing data for TC forecasts. It is organized as follows: Section 2 introduces the GNSS-RS technique, Section 3 reviews the assimilation of GNSS RO data, Section 4 reviews the assimilation of GNSS-R data, and conclusions and prospects are drawn in Section 5.

2. Principles of GNSS Remote Sensing Technique

2.1. GNSS RO

When a low LEO satellite equipped with an RO receiver ascends or descends, the receiver intercepts electromagnetic waves emitted by GNSS satellites that have undergone atmospheric refraction, which constitutes an occultation event [15]. If the atmosphere were a vacuum, the propagation path of the radio signals from the GNSS satellite to the LEO

satellite receiver would be a straight line connecting the two satellites. However, in the real atmosphere, the radio signals bend toward the region of higher atmospheric refractivity, creating a curved path. Due to the density of the atmosphere, the atmospheric refractivity decreases exponentially with altitude, with the refractivity gradient being strongest in the vertical direction. This gradient is primarily influenced by local weather systems, particularly by the water vapor field in the lower troposphere. Consequently, the radio signal path in an occultation event generally bends toward the Earth's surface, with the maximum bending occurring near the point where the path is closest to the Earth's surface. Figure 2 illustrates the principle of RO.

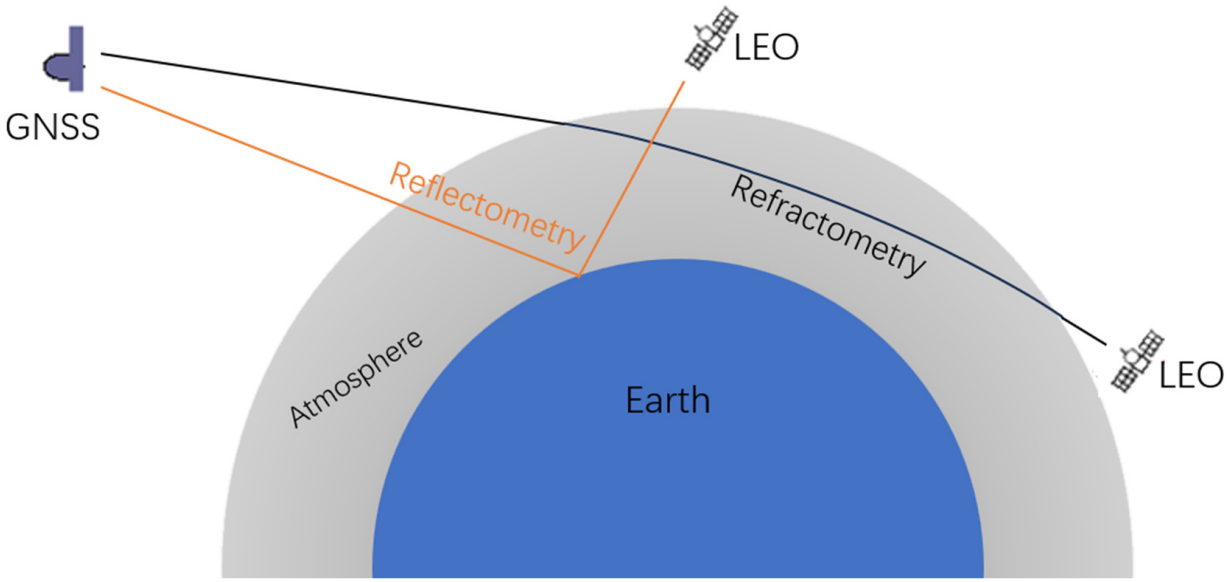

Figure 2. The geometric relations of RO and GNSS-R.

The initial data of RO observation are the variation in optical path lengths at two L band frequencies. Firstly, based on precise orbital positioning and stable atomic clocks, the variation in the optical path length can be used to determine the excess optical path length. The excess optical path length is the difference between the optical path length in the real atmosphere and the vacuum atmosphere, representing the effect of the actual atmosphere on the optical path. Then, under the assumption of spherical symmetry, the excess optical path length can be used in conjunction with satellite geometry to determine the bending angle. After that, through Abel integral inversion (1), the atmospheric refractivity in the vertical can be derived as Equation (1)

$$n(r) = exp\left(-\frac{1}{\pi}\int_r^{\infty}\frac{d\alpha}{dr'}\frac{dr'}{\sqrt{r'^2 - r^2}}\right) \quad (1)$$

where $n(r)$ is the refractivity with r, r is the distance between the Earth's center and observation, and α is the bending angle, which will change by broadcasting through the atmosphere.

If the influence of atmospheric moisture is neglected, the refractivity can be used to calculate the temperature in dry atmospheric conditions using the hydrostatic Equations (2) and (3)

$$\frac{dp}{dh} = -\rho g \quad (2)$$

where p is the atmospheric pressure, h is height, ρ is the density of the atmosphere, and g is gravitational acceleration;

$$N = n \times 10^6 = 77.6\frac{p}{T} \tag{3}$$

where N is the refractivity index, n is the atmospheric refractivity at a certain height, p is atmospheric pressure in mbar, and T is the temperature in Kelvin.

If considering the impact of water vapor, to retrieve the moisture, the relationship among the refractivity index, atmospheric pressure, temperature, and water vapor partial pressure becomes

$$N = n \times 10^6 = 77.6\frac{p}{T} + 3.37 \times 10^5 \frac{e}{T^2} \tag{4}$$

where e is the water vapor partial pressure in mbar. We can analyze a priori temperature field [16] and then use a one-dimensional variational method to obtain the atmospheric profile.

Figure 3 shows examples of GNSS RO profiles of temperature and humidity for tropical cyclones.

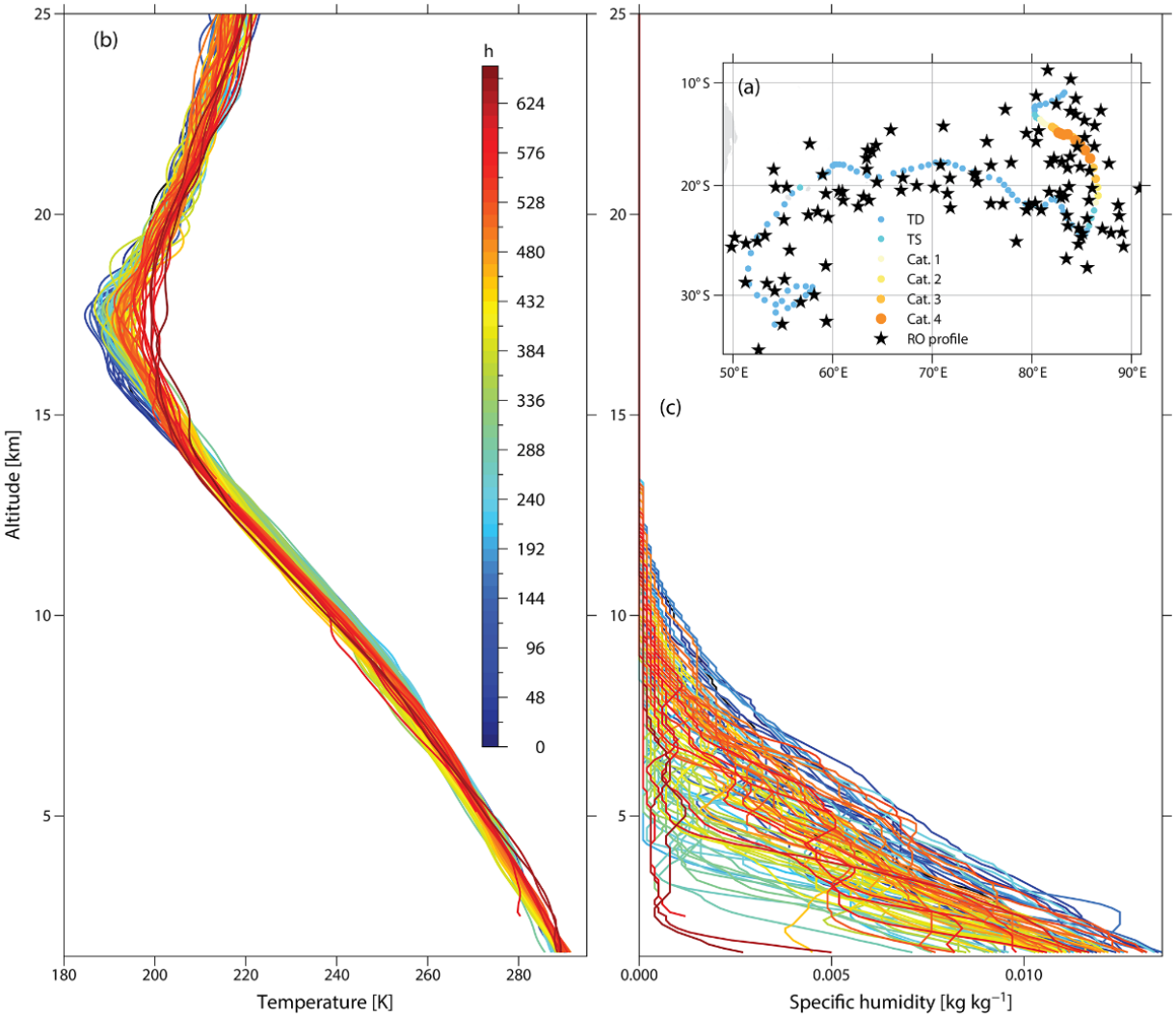

Figure 3. Typhoon Hondo in 2008 best-track and co-located ROs (**a**). TD (tropical depression), TS (tropical storm), and Cat. 1–4 means 1 min maximum sustained wind speed (m/s) $\leq$ 17, 18–32, 33–42, 43–49, 50–58, and 58–70 respectively. From the surface to 25 km altitude temperature (**b**) and specific humidity (**c**) profiles in the storm [17].

2.2. GNSS-R

As the wind blows, the ocean surface becomes rough due to the wind-caused waves. The GNSS satellite signals illuminate the rough ocean surface and diffuse reflection occurs. Actually, we can collect the peak value and shape of the reflection waveform to represent the roughness of the ocean surface. The higher the wind speed, the rougher the ocean surface, leading to more diffuse reflection. At last, it results in the peak value of the waveform reduction and waveform edges being flat [18].

The delay-Doppler map (DDM) shown in Figure 4 is a fundamental physical parameter based on a GNSS-R measurement, and it describes the characteristics of the time and signals. It is generated by cross-correlating the received signal with a replication of the transmitted signal, covering a range of delays and Doppler frequencies. DDM is then calibrated into a bistatic radar cross-section (BRCS) using geometry and the power parameters of the transmitter and receiver

$$\sigma = \frac{P_g (4\pi)^3 (R_r)^2 (R_t)^2 L_{a1} L_{a2}}{P_t \lambda^2 G_t G_r} \tag{5}$$

where σ is the radar cross-section, P_t is the GNSS transmit power, P_g is the noncoherently processed scattered signal power, λ is the GNSS signal carrier wavelength, G_t is the antenna gain of GNSS, G_r is the antenna gain of the receiver, R_r and R_t are the distances to and from the Earth surface, respectively, and L_{a1} and L_{a2} represent the atmospheric losses along the signal's propagation to and from the surface, respectively.

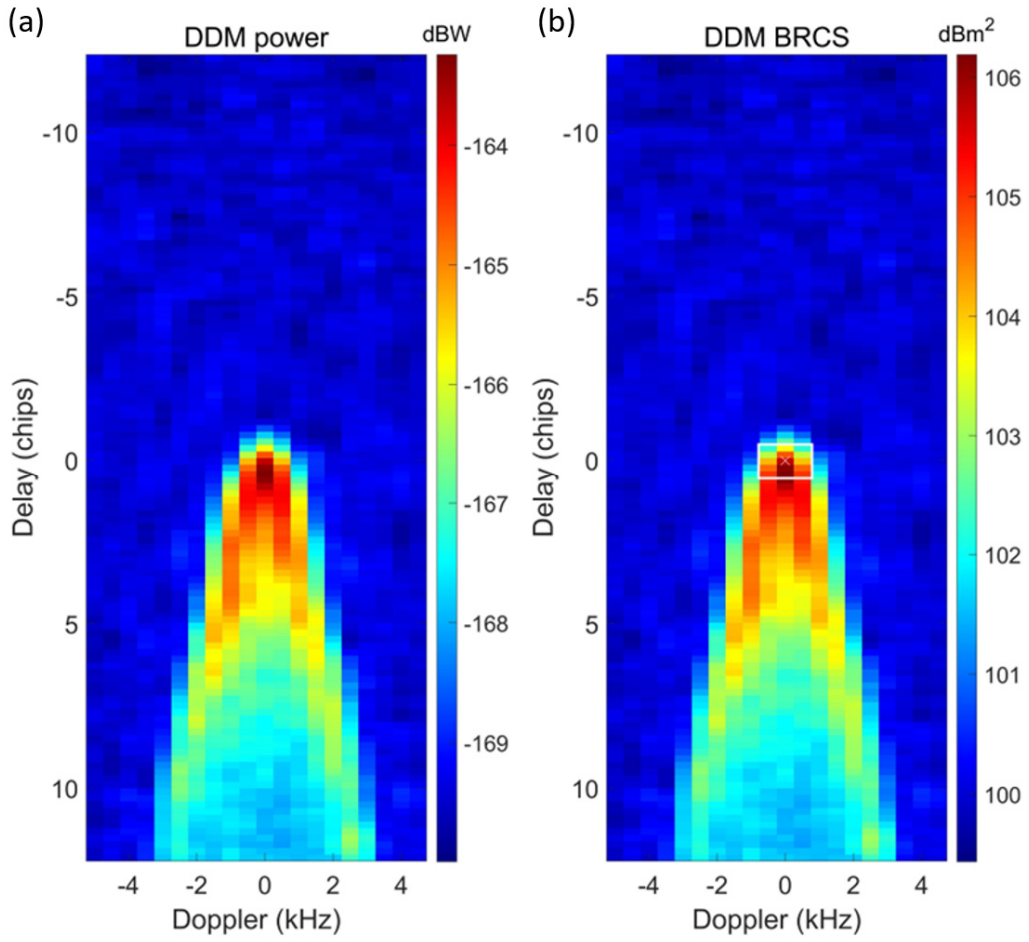

Figure 4. (**a**) Is DDM power, and (**b**) is DDM BRCS. In (**b**), the white rectangle highlights the region of the σ BRCS that can be used for estimating the wind speed. The white X marks the estimated location of the specular bin in the DDM.

To retrieve the ocean surface wind speed from the DDM BRCS, a number of algorithms have been developed [19–21]. Typically, there are two key observables computed using a 3 × 5 delay-Doppler window in DDM, shown in Figure 4b, the normalized bistatic radar cross-section (NBRCS) and leading-edge slope (LES). The center of the window is usually the bin nearest the predicted specular point delay, to catch the peak value of reflection, and the spatial resolution can achieve 25 km [20]. Then, utilizing empirical geophysical model functions (GMFs) that link the surface speed with NBRCs and LES [22–24], we can derive the wind speeds. Figure 5 shows the retrieval results of ocean surface wind speeds from FY-3E for a typhoon in 2023.

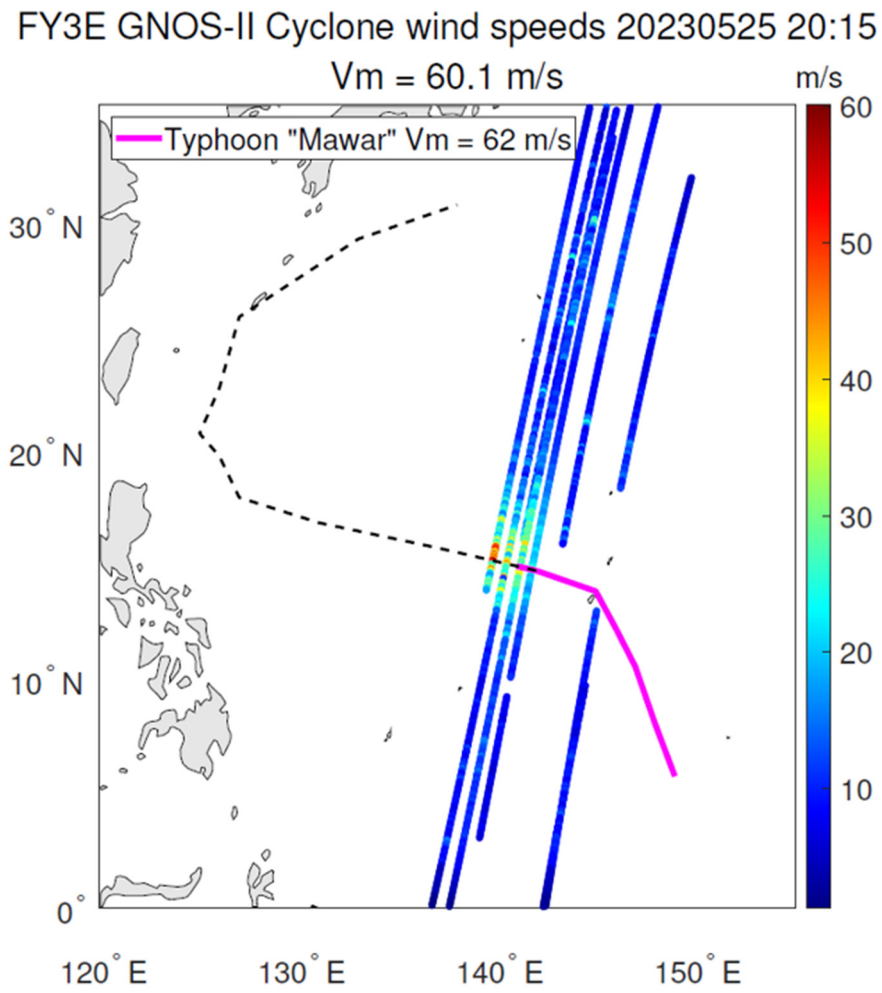

Figure 5. GNSS-R ocean surface wind observations of FY-3E GNOS-II for Typhoon Mawaron 25 May in 2023 [25].

2.3. Spaceborne Missions

The development of GNSS-RO can be traced back to the late 1960s. Initially based on occultation methods used to explore planetary atmospheres, NASA's Mariner 10 mission employed this method to study the atmosphere of Venus [26]. When GPS was launched in 1978, the first GPS meteorology experiment announced RO detecting's growth [27].

The application of occultation observation technology in meteorology started with the 1995 GPS/Meteorology experiment. This experiment marked a significant leap from theory to practice by pioneering the use of the GNSS limb sounding to probe Earth's atmosphere [28]. From April 1995 to March 1997, the GPS/MET [29] satellite collected tens of thousands of occultation profiles. With NASA's help, the first satellite Orsted [30] from Denmark launched in 1999. It had the receiver Turbo-Rogue for GPS signals and could

also obtain the temperature and moisture information vertically through RO detecting. South Africa also launched the Sunsat [31] with Orsted at the same time. By May 2000, the experiment had generated over 80 technical reports and scientific papers, providing the first solid evidence of the accuracy and potential benefits of GPS occultation data. Building on this success, Germany launched the CHAMP [32] mission in July 2000, further advancing the field. From February 2001 to October 2008, the CHAMP satellite delivered around 230 vertical occultation profiles daily, which were crucial for geosciences and atmospheric research. In November 2000, the SAC-C satellite [33], a collaborative effort among Argentina, the U.S., and several other countries, aimed to conduct global limb sounding of the Earth's neutral atmosphere and ionosphere. Following this, in March 2002, the U.S. and Germany launched the GRACE [34] mission, significantly improving geoid measurements from the meter scale to the centimeter scale. The same year, Australia launched FedSat [35]; it received GPS signals to detect the ionospheric electron density and the atmosphere. Germany continued to contribute to the field with the launch of the TerraSAR-X [36] satellite in June 2007, equipped with a high-precision dual-frequency occultation receiver for more accurate orbit determination and atmospheric sounding. Meanwhile, the U.S.–Chinese Taiwan collaboration led to the launch of the COSMIC mission in April 2006, which became a key provider of real-time, high-quality occultation data, crucial for NWP systems [37]. Its successor, COSMIC-2, was launched in June 2019, further enhancing observations, particularly in tropical regions. In addition to these advancements, the European MetOp [38] series of polar-orbiting satellites equipped with GRAS receivers have been providing approximately 600 occultation profiles daily. These data are integrated into NWP systems, alongside satellite microwave and infrared observations, to improve weather forecasts [39]. In addition, Spain's PAZ [40] has great significance for storm forecasting using the polarimetric RO technique. The information near the freezing level could potentially be useful for NWP models when assimilating heavy precipitation data.

In the 1990s, people found that the observation could rely on the GNSS-reflected signals. Martin-Neria proposed the Passive Reflectometry and Interferometry System (PARIS) [41], which had developed into a pristine GNSS remote sensing technique. Both the reflected signal and direct signal are received by the satellite receiver, and the delay of time or phase between them will be used for interferometry. Then, according to the spatial relation of the satellite, receiver, and specular highlight, we can retrieve the characteristics of the Earth's surface, such as sea surface altimetry, which is based on calculating the time delay between GPS direct signals and reflected signals [42]. Foti used the TDS-1 (Technology Demonstration Satellite-1) carrying the receiver SGR-ReSI launched in 2014 for ocean winds [43]. The receiver had obtained a large amount of 2D DDM data that nowadays are often utilized to retrieve the ocean winds.

CYGNSS (Cyclone Global Navigation Satellite System) [44] was launched by NASA in 2016 and is the first GNSS-R mission specifically designed to monitor ocean surface winds, particularly in TC regions, using GNSS signal reflections. In addition to governmental and institutional projects, commercial companies have also entered the field of GNSS-R. Spire GNSS-R consists of a series of CubeSats operated by Spire Global, utilizing GNSS-R technology for Earth observations that includes atmospheric, oceanic, and land surface parameters [45]. HydroGNSS is a mission funded by the European Space Agency (ESA), expected to launch by late 2024 or early 2025 [46].

China has also made significant strides in this area. Since 23 September 2013, the FY-3 series of satellites, equipped with GNOS occultation receivers, have been gradually launched [47,48]. The data collected by these satellites are now utilized by both the China Meteorological Administration (CMA) and the European Centre for Medium-Range Weather Forecasts (ECMWF) for operational assimilation. FY-3/GNOS-II [49], launched in

2021–2023 and operated by the CMA, is the first operational mission that combines GNSS RO and GNSS-R measurements from multiple GNSS constellations. The payload design that integrates GNSS RO and GNSS-R is shown in Figure 6 [50]. This setup marks the first international realization of integrated GNSS RO and GNSS-R remote sensing, enabling the simultaneous acquisition of three-dimensional observational data on the ionosphere, atmosphere, and ocean. To date, more than 5 million occultation event data products have been accumulated, with over 15 million various profile products provided. These data products have passed quality assessments by numerous domestic and international operational and research institutions. The atmospheric occultation refractivity inversion accuracy of the systems compatible with BeiDou and GPS is better than 1% from 10 km to 30 km. These products play a crucial role in global and regional weather forecasting, particularly in regions with high-speed tropical and temperate cyclones, where they exhibit high accuracy. The global ocean surface wind speed data from GNOS-II has been operationally assimilated into the CMA's GRAPES NWP system since May 2023 [25,51], demonstrating a neutral to positive impact on model analysis and forecasting, thereby enhancing the accuracy and reliability of weather forecasts. Except for FY-3, China cooperated with Russia and launched the YH-1/Phobos-Grunt [52] in 2011 for Mars exploration. It used the RO technique to determine the density of electrons in the Martian ionosphere. As for BF-1A/B [53] launched in 2019, people have retrieved ocean surface winds, the sea surface height, and soil moisture using the Earth reflected delay Doppler maps from it. Tianmu-1 [54] is a commercial constellation with 23 satellites launched in 2023–2024 that provides global, all-weather atmospheric, surface, and ocean surface parameter data. Table 1 shows spaceborne GNSS RO and GNSS-R missions in chronological order.

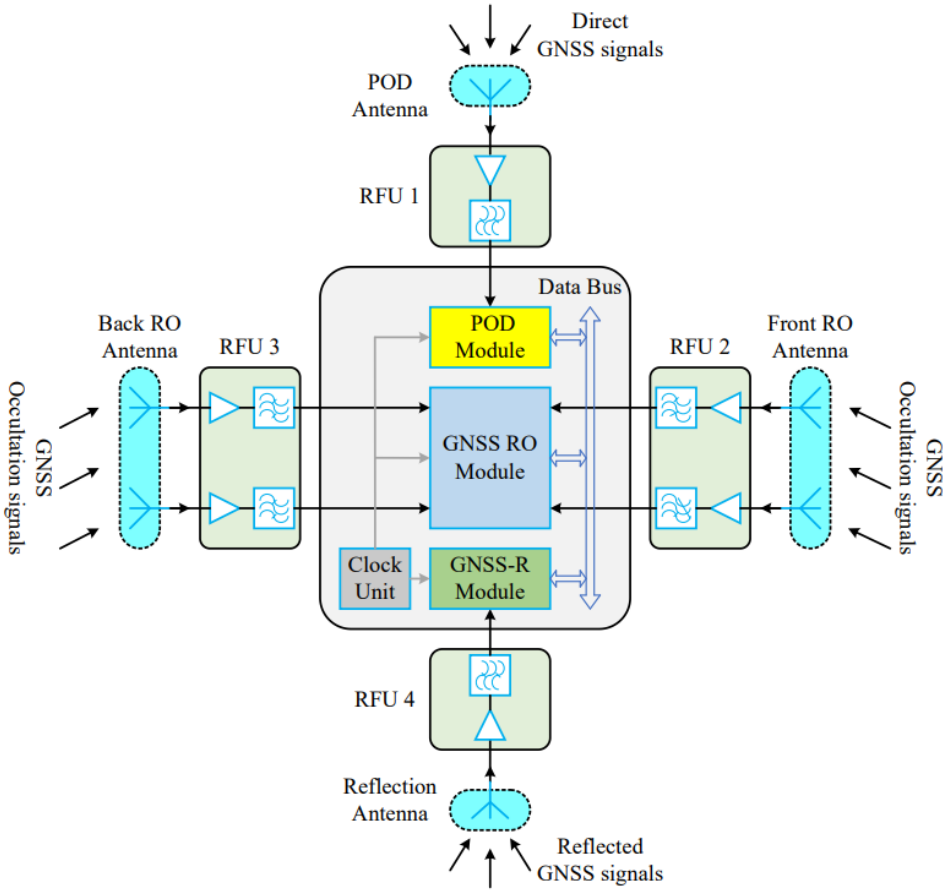

Figure 6. The structure of the spaceborne integrated GNSS remote sensors (SIGRS) for FY-3E/GNOS- II [50].

Table 1. List of spaceborne GNSS RO and GNSS-R missions.

Mission Name	Country	Task	Launch Time
GPS/MET	USA	GNSS RO	1995
Orsted	Danmark	GNSS RO	1999
Sunsat	South Africa	GNSS RO	1999
CHAMP	Germany	GNSS RO	2000
SAC-C	Argentina	GNSS RO	2000
GRACE	Germany	GNSS RO	2002
FedSat	Australia	GNSS RO	2002
UK-DMC	UK	GNSS-R	2003
COSMIC	USA/Chinese Taiwan	GNSS RO	2006
MetOp	Europe	GNSS RO	2006
TerraSAR-X	Germany	GNSS RO	2007
OCEANSAT-2	Italy	GNSS RO	2009
TanDEM-X	Germany	GNSS RO	2010
YH-1/Phobos-Grunt	China/Russia	GNSS RO	2011
KOMPSAT	Korea	GNSS RO	2013
FY-3C/D	China	GNSS RO	2013
TDS-1	UK	GNSS-R	2014
CYGNSS	USA	GNSS-R	2016
PAZ	Spain	GNSS RO	2018
BF-1A/B	China	GNSS-R	2019
FSSCAT	Europe	GNSS-R	2020
FY-3E/F/G	China	GNSS RO/GNSS-R	2021
Spire	USA	GNSS RO/GNSS-R	2021
Tianmu-1	China	GNSS RO/GNSS-R	2023–2024

3. Assimilation and Impact of GNSS RO Data

TCs are typically deep convections, where the height and temperature of the cloud tops are usually associated with the strength of the system [55,56]. Currently, approximately 20,000 RO data points are assimilated globally every day [57], but it is also a challenge to obtain high vertical resolution and high-accuracy atmospheric temperature and water vapor profile observations near the tropopause, especially in severe weather conditions, such as TCs. In applied early operational forecasting of RO data, only data above an altitude of 4 km were used. Nowadays, most operational centers still do not assimilate RO data below the atmospheric ducting/trapping layer, which is characterized by large gradients in atmospheric refractivity and water vapor in the lower troposphere. However, lower-level RO observations, particularly in tropical regions, contain valuable information about atmospheric moisture, making their application extremely important. All-weather atmospheric information, especially near-surface data under cloudy or rainy conditions, is crucial for studying and validating theories on the genesis and evolution of TCs.

In fact, RO data are highly accurate in the upper troposphere and lower stratosphere (UTLS), and many studies have utilized these observations to investigate deep convection in the UTLS, such as the structure of TCs, and cloud top heights [58]. Biondi et al. [59] determined cloud top heights using the peak of RO bending angle anomalies and validated their findings with data from the Cloud-Aerosol Lidar and Infrared Pathfinder Satellite Observations (CALIPSO) and the International Satellite Cloud Climatology Project (ISCCP). They then utilized RO data to explore the vertical structure of TCs and analyzed the specific relationship between the cloud top height and TC intensity [60]. We can see the difference between the RO cloud top heights and the altitudes of the troposphere in Figure 7.

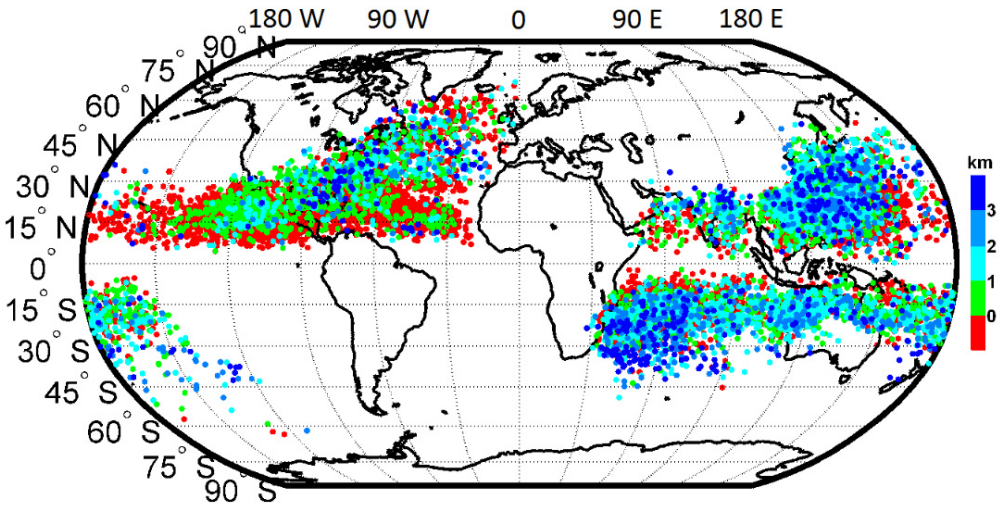

Figure 7. Difference distribution between the cloud top heights and the tropopause altitudes in GPS RO profiles with TC best tracks [58].

3.1. Method of Assimilating GNSS RO Data

For assimilating GNSS RO data, here are several methods. The assimilation systems in forecast models have some generic and popular approaches, including 3DVAR, 4DVAR, and ensemble Kalman filters (EnKF), for both RO data and GNSS-R data [61–63]. 3DVAR uses observations and background in models to adjust analyses. It has nice stability and high computational efficiency, but due to the ignoration of time, its dynamic constraints are weak. 4DVAR added the time dimension to capture the rapid changes effectively. However, it is sensitive to background errors and costs many computational resources. ENKF, based on statistics methods, makes the background errors more suitable to the real atmosphere, but the ensemble size is limited by the resources. Here is also a choice to combine the EnKF's background errors and the variational assimilating method to improve the results flexibly [64]. As for the operators [65], firstly, we could use 1DVAR to retrieve the atmospheric temperature and moisture profiles, and then assimilate the physical information to NWP. In addition, with the application of a forward operator and adjoint operator [66], choosing the refractivity or bending angle to replace moisture and temperature could also affect the results of assimilation. The refractivity includes the local and non-local refractivity [67,68], and the bending angle [69,70] could be derived by the ray tracer, a model of simulating the local bending angle [71] under Snell's Law.

The refractivity local operator relies on a certain position in the atmosphere, which could simplify the computation. However, the non-local operator would consider the whole signal path, and it captures the cumulative refraction effects across various atmospheric layers on the entire signal propagation path. So, it is significant to perform the global vertical structures [17]. Also, the non-local refractivity operator provides a way to derive the bending angle. Different bending angle ray tracers [72] are adapted to different atmosphere assumptions. If there is a single point in the atmosphere or at a certain height, the local bending angle operator is suitable for estimating the bending angle using less computational cost. 2D ray tracer is for a symmetric and uniform atmosphere, where the refractivity, temperature, and moisture are changed with the altitude but not distance horizontally [73]. This means that the signal propagates straightly. The bending angle 3D ray tracer could describe the atmospheric changes in both directions, and it could be used in complex situations, such as the unsymmetric temperature gradient. According to the computing resources and the forecasting problems, we could choose different settings.

3.2. Impact of GNSS RO Data

Teng utilized COSMIC-2 data by assimilating GNSS RO data with the Weather Research and Forecasting (WRF) model, resulting in a false alarm ratio reduction by 20% and an accuracy rate enhancement by 19% [74], as shown in Table 2. The TC formation mentioned here is the prosperity of a tropical cloud cluster (TCC) into a TC. For each TCC, two experiments were conducted: GTS, with the assimilation of NCEP conventional observation data, and EPH, along with the conventional observations, there was the assimilation of a non-local excess phase operator [75] of GNSS RO data. Miller [76] evaluated the impact of assimilating RO bending angles from COSMIC-2 on Hurricane Weather Research and Forecasting (HWRF) TC forecasts. The results showed that COSMIC-2 assimilation led to a significant 8–12% reduction, statistically, in the mean absolute error for the minimum central ocean level pressure in lead times of 36, 54, 60, and 108–120 h forecasts. Figures 8 and 9 illustrate that the area near the Central American landmass seemed to be the origin of low-to-mid-troposphere dry air intrusion, which invaded the Zeta circulation on the eastern side in the beginning 18 h of the free forecast. This dry air intrusion was more obvious in the C2 experiment, identical to the analysis differences. The difference between the C2 and Control experiment was the assimilation of COSMIC-2 bending angles. The Control assimilated all obtainable observations and excluded RO data, while the C2 involved the COSMIC-2 bending angles. Mueller [77] utilized simulated refractivity with conventional observations, such as radiance, temperature, and humidity, to perform a cycle forecast experiment and then assessed the potential impact on the TC track, maximum ocean surface wind speed, and integrated kinetic energy (IKE) forecasts. The results indicated that the global track forecasts have little relationship with GNSS RO data, but the wind speed and IKE forecasts had been actually slightly degraded at the lead time of 30 h to 60 h. Masaru [78] assimilated simulated low-latitude GPS RO refractivity using a mesoscale 4-dimension variational data assimilation system and found that RO data with robust characteristics and high accuracy are profitable for the TC forecast presented in Figures 10 and 11. Experiment MA_RO assimilated GPS RO data; additionally, it performed more specifically in TCs' structure and was more similar to the best track. Chen's study showed the impact of assimilating GNSS RO local refractivity and the bending angle on a typhoon that passed over Chinese Taiwan [79]. The forecast results at a 60–15 km resolution revealed that GNSS RO data actually improved the prediction of the TC track, as shown in Figure 12. Compared with refractivity, assimilation with bending angles had better performance, particularly for wind. In the experiments, NODA had no assimilation, GTS assimilated conventional data and satellite radiance without GNSS RO data, REF was GTS with GPS refractivity data, and BND was GTS with GPS bending angle data. For precipitation, we could see in Figure 13 that GNSS RO data helped a lot in finding the center location of the maximum rainfall but still had the potential to forecast the precipitation altitude.

Summarizing the above cases, we also found that the forecasts at the initial time of mid-level moisture around the disturbance centers were increased after the assimilation of GNSS RO data. For developing cases, it also increased low-level vorticity, while for non-developing cases, it reduced vorticity throughout most of the troposphere. The current NCEP forecast system showed that the impact of COSMIC-2 RO data on NWP is significant in the upper troposphere and lower stratosphere [80], similar to analyses from the U.S. Navy system [81] and the ECMWF system. However, ECMWF also showed that GNSS RO data had improved the moisture and precipitation forecasts below a 5 km altitude [82], although there appeared to be considerable uncertainty in the troposphere below a 2 km altitude.

Table 2. 2 × 2 contingency tables and various skill scores of TC forecasts formation for GTS (assimilating conventional data) and EPH (GNSS RO data in addition to GTS). Hit rate: hits/(hits + misses). Specificity: correct negatives/(false alarms + correct negatives). False alarm ratio: false alarms/(hits + false alarms). False alarm rate: false alarms/(false alarms + correct negatives). Bias score: (hits + false alarms)/(hits + misses). Accuracy rate: (hits + correct negatives)/(hits + misses + false alarms + correct negatives). Threat score: hits/(hits + misses + false alarms). Sensitivity to RO: proportion of GNSS RO data assimilation improved performance cases in total categories [74].

		Observation		Total	Hit Rate	Specificity	False Alarm Ratio	False Alarm Rate	Bias Score	Accuracy Rate	Threat Score
		Developing	Non-Developing								
GTS Forecast	Detected	4 (hits)	11 (false alarms)	15	0.44 *	0.52 *	0.73 *	0.48 *	1.67	0.50 *	0.20 *
	Non-detected	5 (misses)	12 (correct negatives)	17							
EPH Forecast	Detected	7 (hits)	8 (false alarms)	15	0.78 *	0.65 *	0.53 *	0.35 *	1.67	0.69 *	0.41 *
	Non-detected	2 (misses)	15 (correct negatives)	17							
Total		9	23	32	/	/	/	/	/	/	/
Sensitivity to RO		0.33	0.13	0.19	/	/	/	/	/	/	/

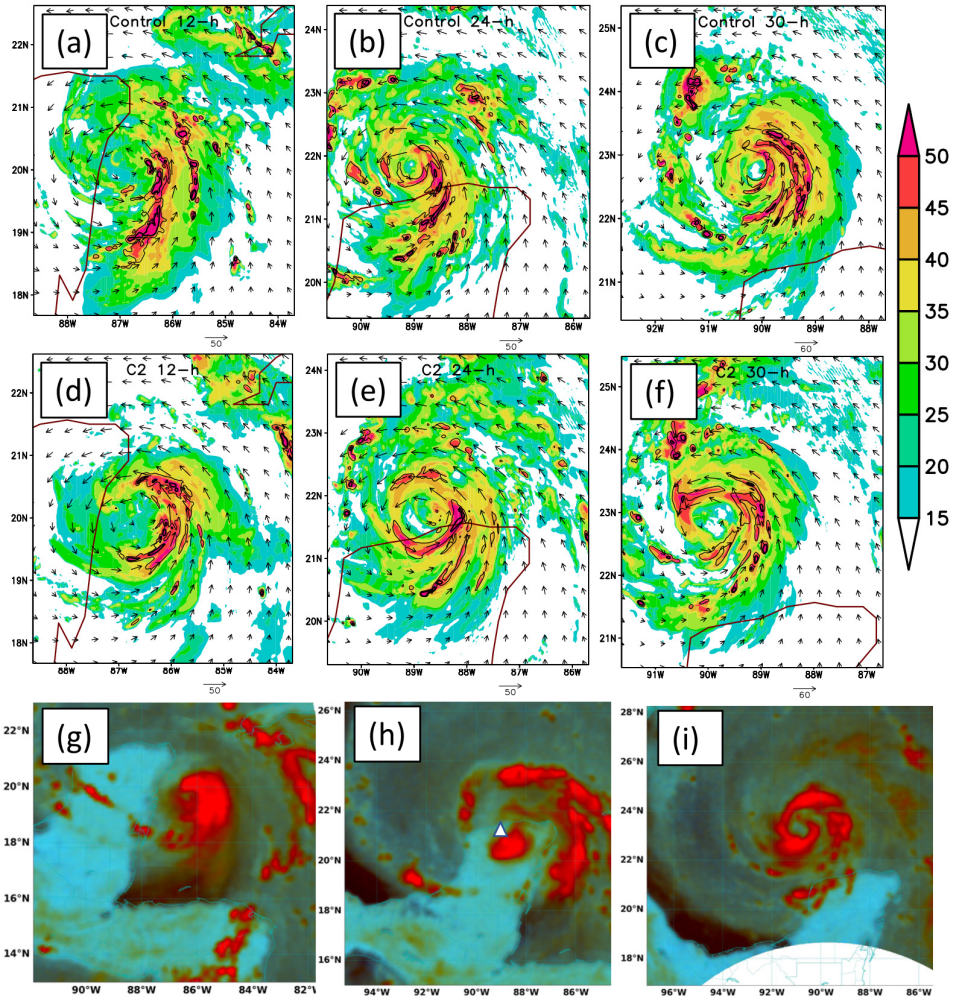

Figure 8. (**a**–**c**) The Control Hurricane Zeta forecasts initialized at 1200 UTC 26 Oct, respectively, at 12, 24, and 30 h. (**d**–**f**) The C2 (Control with RO bending angle) Hurricane Zeta 12, 24, and 30 h forecasts initialized at 1200 UTC 26 Oct, respectively. (**a**–**f**) figures have horizontal wind vectors on the forecasts. (**g**–**i**) SSMIS 91-GHz color composite imagery, at 2225 UTC 26 Oct, 1058 UTC 27 Oct, and 0030 UTC 28 Oct, respectively. In (**h**), the NHC best track center is marked by a white triangle at 1200 UTC 27 Oct (21.38N, 89.08W) [76].

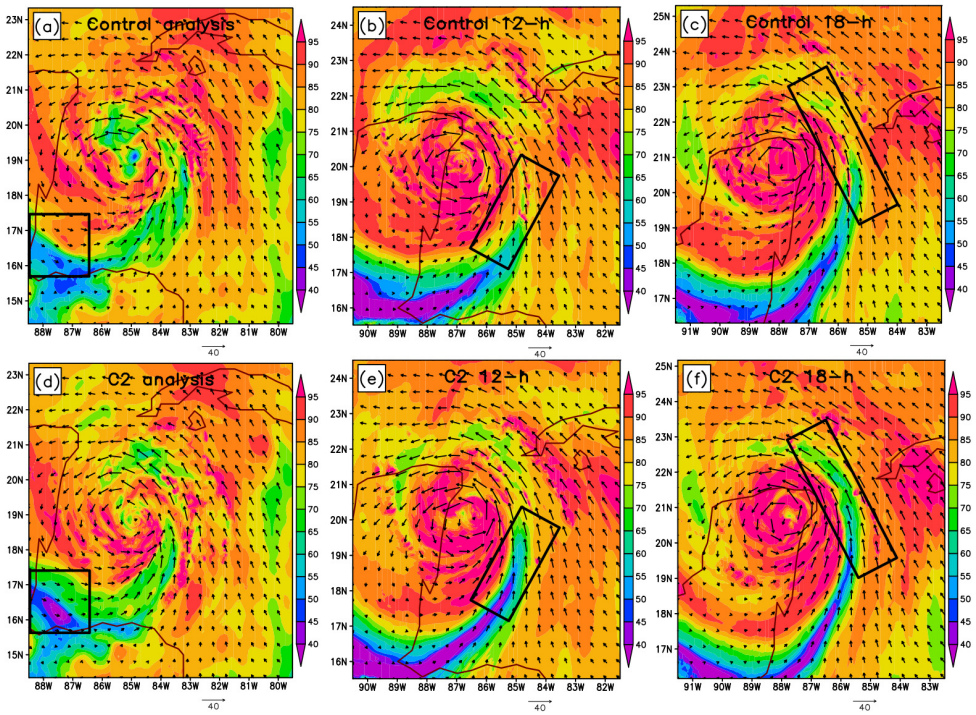

Figure 9. (**a**) The HWRF Control Hurricane Zeta horizontal wind vectors (m/s) at 750 mbar with layer-averaged RH (shade, %) at 700–800 mbar from the cycled analysis initialized at 1200 UTC 26 Oct. (**b**,**c**) As in (**a**), but for the 12 and 18 h verification times, respectively. (**d**–**f**) As in (**a**–**c**), but for the HWRF C2 forecast. The dry tongue is highlighted by the black rectangular boxes [76].

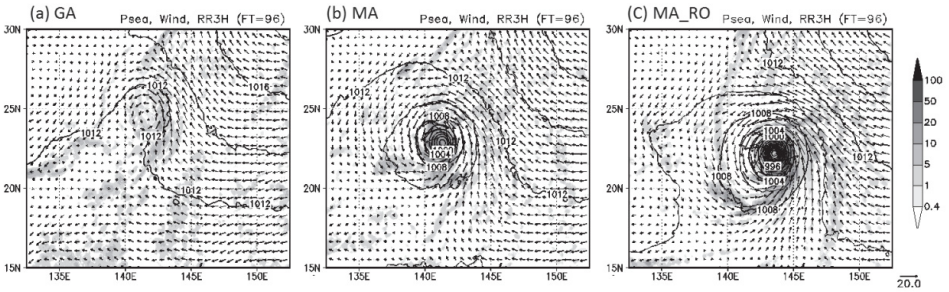

Figure 10. (**a**–**c**) is for GA (the JMA global analysis), MA (analysis by the Meso 4D-Var system), and MA_RO (the same as MA but RO data were assimilated additionally), the distributions of sea-level pressure (hPa), surface wind vectors (m/s), and accumulated precipitation (shade, mm) in a 3 h period at 0000 UTC 31 July 2007 from NHM forecasts using different background fields [78].

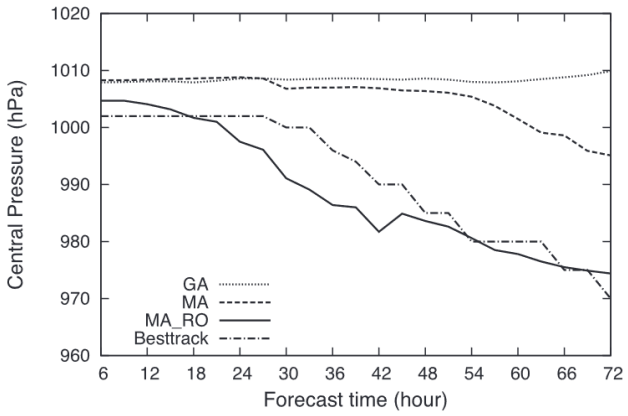

Figure 11. Time series of the central pressure predicted by NHM of typhoon Usagi, for GA, MA, MA_RO, and Besttrack data [78].

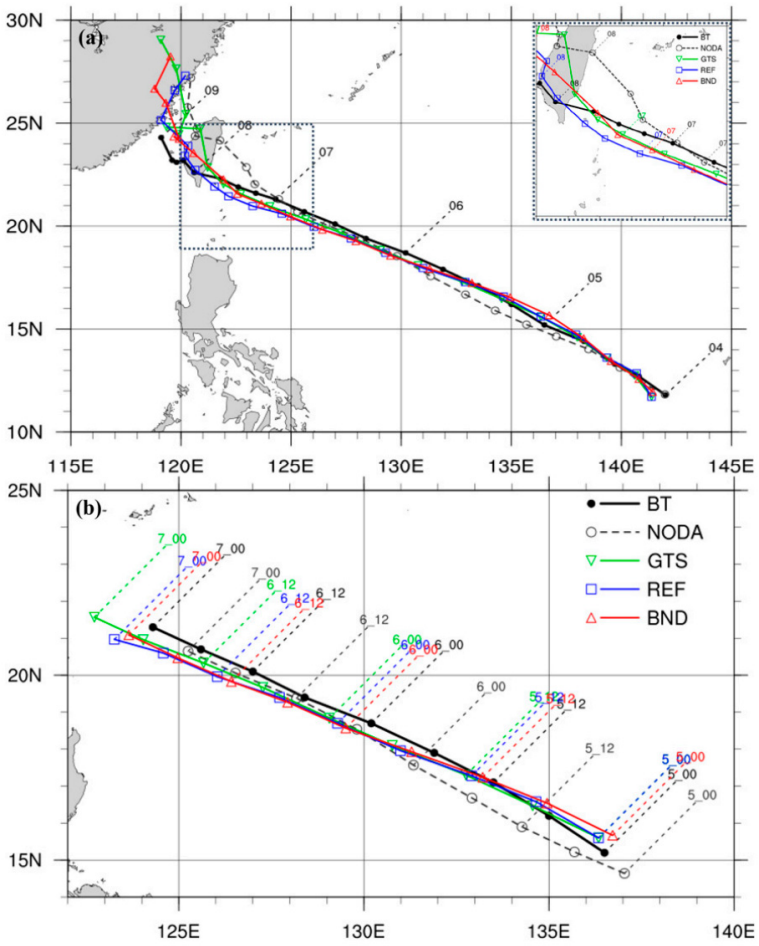

Figure 12. (**a**) The black dot is the best track from observations, and others are the simulated tracks for NODA (the initial condition from NCEP), GTS (assimilating conventional and satellite radiance data), REF (GTS along with RO refractivity), and BND (GTS along with RO bending angle), respectively. The area in the dashed square is zoomed as shown at the upper-right corner with the details of the tracks. (**b**) As in (**a**), but the tracks during 5–7 Jul [79].

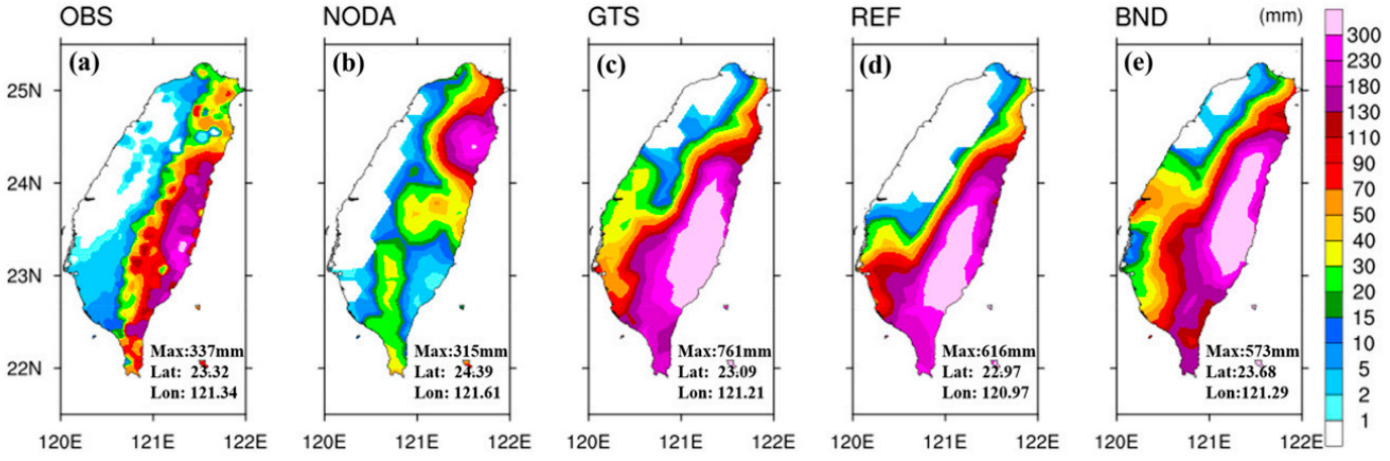

Figure 13. (**a**) Observation, (**b**) NODA, (**c**) GTS, (**d**) REF, and (**e**) BND, the accumulated rainfall (mm) during 0000 UTC 7–8 Jul 2016. Text at the bottom right is the location and amount of the maximum rainfall (mm) [79].

4. Assimilation and Impact of GNSS-R Data

Compared to atmospheric profiles provided by GNSS RO, ocean surface winds observed by GNSS-R are more visually interpretable and thus can provide direct information on the location, intensity, and structure of TCs. Therefore, GNSS-R wind data can be used to directly monitor TCs [83–85]. To improve TC forecasts of NWP models, GNSS-R wind observations need to be assimilated into NWP models. GNSS-R wind speeds can modify the first guess through assimilation and then improve forecasting. NASA's CYGNSS constellation, consisting of eight satellites, aims to use GNSS-R ocean surface wind observations to improve the trajectory and intensity forecasts of TCs. This assimilation can significantly impact the accuracy of weather forecasts and climate models [79–83]. By integrating these data, we can more accurately understand and predict extreme weather events, like TCs, thereby enhancing the reliability of forecasts.

4.1. Method of Assimilating GNSS-R Data

Methods of assimilating GNSS-R ocean surface wind data are generally similar to those of assimilating conventional wind observations. Due to the characteristics of GNSS-R signals, they usually have no wind direction information. A Variational Analysis Method (VAM) can combine GNSS-R wind speeds with wind vectors offered by a priori background and completes a near-surface vector wind field. Studies have shown that using assimilation systems and the VAM to assimilate either simulated or actual CYGNSS wind speed data is effective [86,87]. Except the VAM, we can also just assimilate the retrieved ocean surface wind speeds without directions. In addition, a popular assimilation method to improve forecasts is data thinning. GNSS-R ocean surface wind speed observations are crowded, with a distance of 6 km between each point, which is much smaller than the model resolution. Therefore, data thinning is usually implemented to avoid overfitting. Typically, we either select the nearest observation to the grid center or use the average of all GNSS-R data points within the grid for assimilation. The difference between these methods will be described next.

4.2. Impact of GNSS-R Data

A number of Observing System Simulation Experiments (OSSEs) have been conducted to validate the impact of assimilating GNSS-R data on typhoon forecasting [86–89]. OSSEs involve comparing the forecast outcomes with and without the assimilation of GNSS-R data. GNSS-R winds are simulated from a hurricane nature run (NR) that is realistic, with the error characteristics probably presenting in reality. This method helps determine the effectiveness of GNSS-R data in improving the accuracy and reliability of TC track and intensity predictions, thereby assessing its operational value in meteorological applications.

McNoldy assimilated CYGNSS wind speeds using the Gridpoint Statistical Interpolation 3-Dimensional Variational (GSI-3DVAR) system, so that the TC structure, intensity, and position, together with large-scale variables, were all enhanced. The results highlighted the potential value of CYGNSS ocean surface wind speed data, and incorporating directional information can further enhance the accuracy of TC analyses and forecasts [89]. Zhang utilized the HWRF model and GSI system to evaluate the influence of assimilating CYGNSS ocean surface winds in a regional OSSE framework. The results revealed that adding GYGNSS data can actually improved the simulation's representation of the TC track and intensity, especially for the accuracy of ocean surface winds, inner-core structures, and surface fluxes forecasts. During the entire 72 h simulation, the minimum sea level pressure (MSLP) and surface maximum wind (MSW) errors had a 23% and 40% reduction, respectively, compared with the control experiment [88]. Figure 14 shows the time series of MSLP and MSW and also gives a track error bar of the experiments. Leidner assimilated

simulated VAM-CYGNSS wind vectors using the GSI 3DVAR system and HWRF model. The results indicated that the assimilation of VAM-CYGNSS wind vectors had reduced the MSW error by 2–5 kt (1 kt = 0.51 m/s) and reduced the MSLP error by 2–5 hPa [86]. The elevation in the intensity forecast was more significant than the reduction of the track error, and the improvement was also more consistent. Annane's experiments were similar to the above; the OSSE framework made use of the HWRF model and GSI system. To estimate the impact of assimilating CYGNSS winds and the difference in whether to add wind directions, CYGNSS winds were separated into scalar winds and wind vectors. In the simulation, the data assimilation cycles of 1, 3, and 6 h intervals were tested. At last, the 3 h interval assimilation was consistently best. In addition, CYGNSS scaler wind speeds improved the intensity forecasts in the first 48 h, resulting in a 2–5 hPa reduction for MSLP and a 2–6 kt elevation for MSW. As shown in Figure 15, the assimilation of CYGNSS wind vectors had a more significant effect on the 10 m wind field and structures in the HWRF model than assimilating wind speeds alone [87].

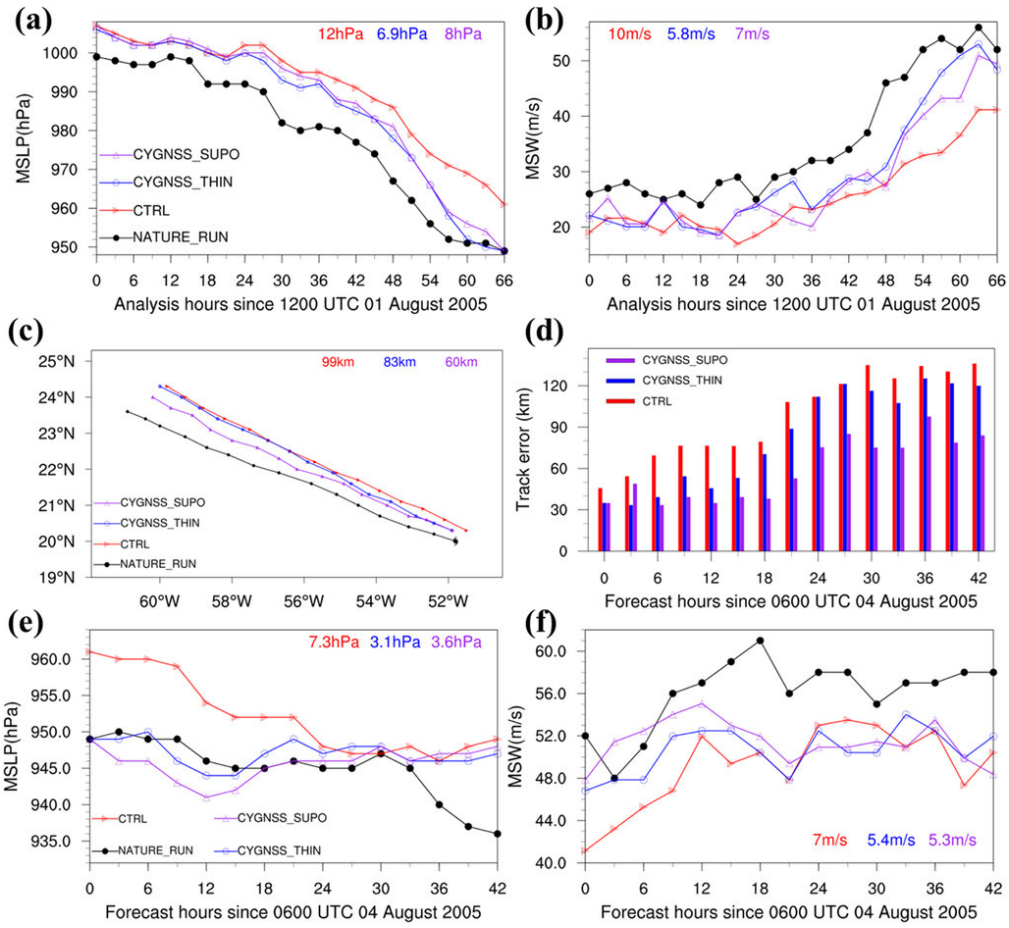

Figure 14. (**a**,**b**) are time series of MSLP and MSW, respectively, during the cycled DA period, 1200 UTC 1 to 0600 UTC 4 Aug 2005. Red for CTRL (assimilating simulated conventional observations), pink and blue for GYGNSS SUPO (CTRL plus CYGNSS speeds and thinning data to one per grid box, closest point kept) and THIN (SUPO but speeds averages kept), respectively, and black for NR. (**c**–**f**) As in (**a**,**b**), but for track, track errors, MSLP, and MSW, respectively, between 0600 UTC 4 and 0000 UTC 6 Aug 2005. Different colored numbers mean the absolute error average of track and intensity in the whole analysis or simulation [88].

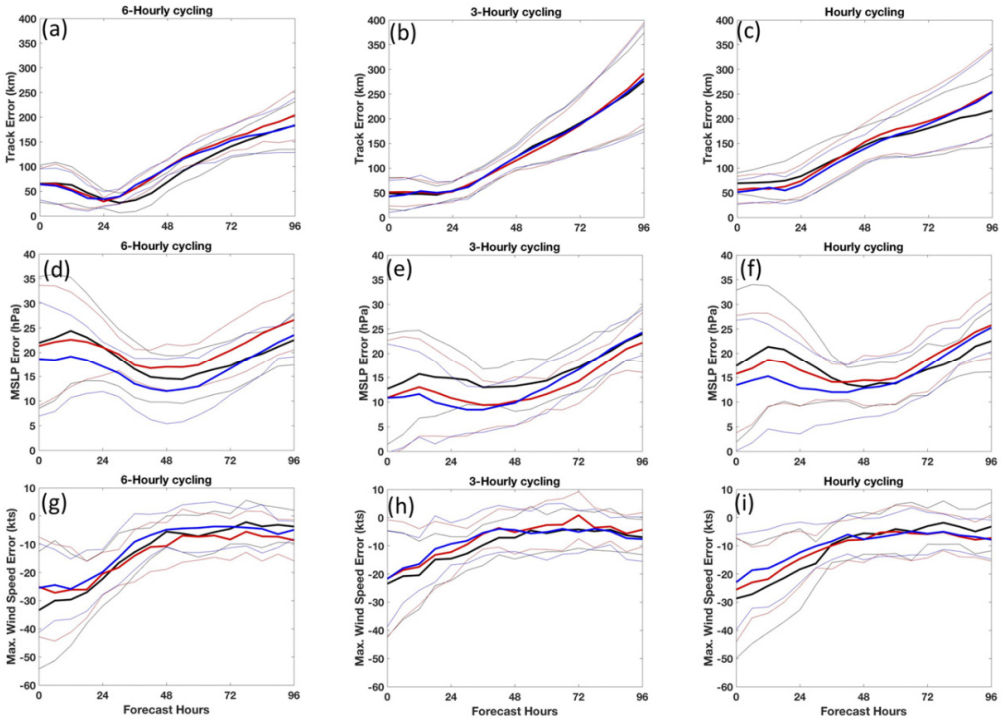

Figure 15. (**a**,**d**,**g**) 6 h; (**b**,**e**,**h**) 3 h; and (**c**,**f**,**i**) 1 h DA cycling experiments for average storm forecast error. Averaged errors/deviations are colored by OSSE experiment: CNTL (conventional observation assimilated) is black/gray, CYG (CNTL plus CYGNSS speeds) is red/light red, and VAM (CNTL plus CYGNSS VAM vectors) is blue/light blue [87].

There are also studies that assimilate real CYGNSS wind speed observations in Observing System Experiments (OSEs). Li employed the WRF Data Assimilation (WRFDA) system, integrating 3D and 4D hybrid variational techniques, to assimilate CYGNSS wind speed during the Madden–Julian oscillation (MJO) event over the Indian Ocean. In Figures 16 and 17, the results indicated that CYGNSS data had a positive impact on wind fields [90]. However, the influence of CYGNSS data rapidly diminished within 4 h after assimilation. Furthermore, CYGNSS data had a limited impact on precipitation forecasts. Mueller assimilated the CYGNSS scalar winds and vector winds utilizing a global data assimilation and forecasting system and found, in the first 60 h, a significant track forecasting improvement of 20–40 km. In the forecast of MSW, a few degradations of 2 kt would appear at some lead times, especially at the beginning of 24 h [91], but at most lead times, there was no statistically significant impact. Pu's experiments were performed using the HWRF model and a GSI- 3DEnVar system [92]. Compared with the influence of Advanced Scatterometer (ASCAT) wind, assimilating CYGNSS data into a hurricane-forecasting model could refine track and intensity forecasts at the beginning of the simulation (within 48 h) with a suitable thinning distance application. Furthermore, the inner-core symmetric structure forecasts performed better when using the CYGNSS data.

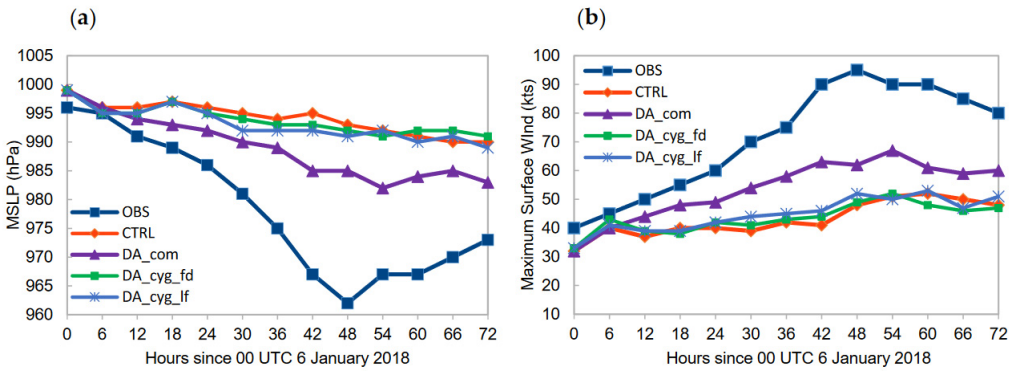

Figure 16. TC intensity in time series for (**a**) MSLP and (**b**) MSW from JTWC best track data, CTRL (a WRF regional simulation), DA_cyg_fd (assimilating CYGNSS fully developed seas wind speed), DA_cyg_lf (assimilating CYGNSS young seas/limited fetch wind speed), and DA_com (assimilating combined IMERGE rainfall, ASCT vector wind, and CYGNSS wind speed) at 0000 UTC on 6–9 January 2018 [90].

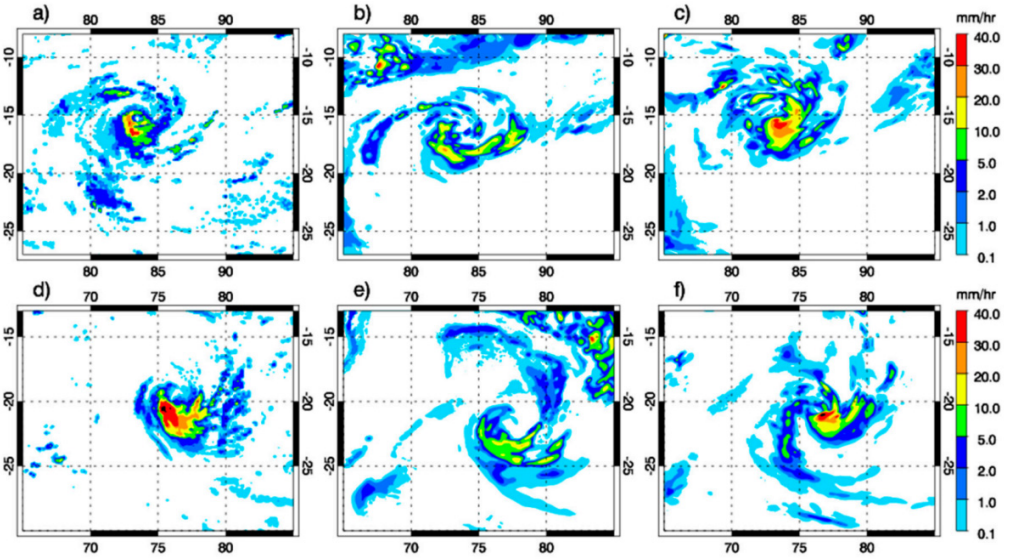

Figure 17. (**a**) IMERG (Integrated Multi-satellitE Retrievals for GPM data), (**b**) CTRL, and (**c**) DA_com precipitation around the TC center at 1500 UTC on 7 January 2018; (**d**–**f**) as in (**a**–**c**), but at 2100 UTC on 8 January 2018 [90].

5. Discussion

Tables 3 and 4 summarize the studies of assimilating GNSS RO and GNSS-R data, respectively. In summary, both GNSS RO data and GNSS-R data have positive impacts on TC forecasting, although they influence different aspects of forecasts. We cannot compare the assimilation results between RO data and GNSS-R data directly as there are no data aiming at the same TC, and the type or size of data are not comparable either. However, in a comparison of Tables 3 and 4, we can find that RO data contribute to moisture and precipitation forecasts more effectively than GNSS-R data. Only combined with other observations, GNSS-R winds will positively impact precipitation forecasting. For the TC track and intensity, both can improve the accuracy of forecasts, but RO data perform better in track forecasting, while GNSS-R data contribute more to the TC intensity forecasting. This is because RO data have a high resolution in vertical and can characterize atmospheric circulation in more detail, and GNSS-R data convey more ocean surface information, such as the major factor of intensity, the surface wind speed.

Table 3. Summary of studies assimilating GNSS RO data.

Title	NWP Model and DA System	Assimilation Method	Impact
Potential Impacts of Radio Occultation Data Assimilation on Forecast Skill of Tropical Cyclone Formation in the Western North Pacific [74]	WRF, 3DVAR	Using nonlocal excess phase operator of GNSS RO data	RO data had an impact on moisture forecasts, and increased low-level vorticity for developing cases.
Evaluating the Impacts of COSMIC-2 GNSS RO Bending Angle Assimilation on Atlantic Hurricane Forecasts Using the HWRF Model [76]	HWRF, 3DEnVAR	With local forward operator NCEP Bending Angle Model (NBAM)	RO data assimilation were more effective in correcting water vapor bias.
Impact of Refractivity Profiles from a Proposed GNSS-RO Constellation on Tropical Cyclone Forecasts in a Global Modeling System [77]	GDAS/GFS, 3DEnVAR	Using simulated RO refractivity from nature run	RO data had more effects on wind speed and IKE forecasts than global track forecasts.
Impact of Assimilation of GPS Radio Occultation Refractivity on the Forecast of Typhoon Usagi in 2007 [78]	JMA, 4DVAR	Using RO refractivity	RO data had a positive impact on the forecast of a TC at the formative and developing stages and improved the dynamic fields.
An Impact Study of GNSS RO Data on the Prediction of Typhoon Nepartak (2016) Using a Multiresolution Global Model with 3D-Hybrid Data Assimilation [79]	MPAS, 3DVAR/EnKF	With local RO refractivity and bending angle operators	Assimilation with bending angle had better performance than refractivity, in particular for the wind forecast.
Understanding the impact of assimilating FORMOSAT-7/COSMIC-2 radio occultation refractivity on tropical cyclone genesis: Observing system simulation experiments using Hurricane Gordon (2006) as a case study [93]	WRF, 3DVAR	Refractivity profiles	Assimilating RO data helped to capture the genesis and development in TC's core region with abundant moisture and vorticity.
Impacts of Radio Occultation Data on Typhoon Forecasts as Explored by the Global MPAS-GSI System [94]	MPAS, 3DVAR/EnKF	Local bending angle and refractivity	The TC track prediction was improved with RO data, especially using bending angle data, but RO data had fewer impacts on the TC intensity forecasts.

Table 4. Summary of studies assimilating GNSS-R ocean surface wind data.

Title	NWP Model and DA System	Simulated or Real Observations	Assimilation Method	Impact
Impact of Assimilating CYGNSS Data on Tropical Cyclone Analyses and Forecasts in a Regional OSSE Framework [89]	WRF, 3DVAR	Simulated	Only wind speed was assimilated, thinning to the grid	CYGNSS surface wind data could improve the analyses of the TC position, structure, and intensity.
Impact of CYGNSS Ocean Surface Wind Speeds on Numerical Simulations of a Hurricane in Observing System Simulation Experiments [88]	HWRF, 3DVAR	Simulated	Only wind speed was assimilated	CYGNSS winds had great potential to improve hurricane track and intensity simulations.

Table 4. *Cont.*

Title	NWP Model and DA System	Simulated or Real Observations	Assimilation Method	Impact
Variational Analysis of Simulated Ocean Surface Winds from the Cyclone Global Navigation Satellite System (CYGNSS) and Evaluation Using a Regional OSSE [86]	HWRF, 3DVAR	Simulated	VAM vectors used for assimilation	CYGNSS winds improved intensity and track forecasts, especially for intensity. VAM-CYGNSS wind vectors played a more effective role in forecasting structures.
A Study of the HWRF Analysis and Forecast Impact of Realistically Simulated CYGNSS Observations Assimilated as Scalar Wind Speeds and as VAM Wind Vectors [87]	HWRF, EnKF/3DVAR	Simulated	VAM vectors used for assimilation	VAM CYGNSS vectors improved the TC intensity and structure forecasts more than only assimilating CYGNSS wind speed.
A Study on Assimilation of CYGNSS Wind Speed Data for Tropical Convection during 2018 January MJO [90]	WRF, 4DEnVAR	Real	Only wind speed was assimilated, with inflated observation errors by a factor of 5	CYNSS data had a positive impact on the TC intensity and track forecasts and also improved wind and precipitation fields when assimilated with combined satellite data.
Impact of CYGNSS-Derived Winds on Tropical Cyclone Forecasts in a Global and Regional Model [91]	HWRF, 3/4DEnVAR	Real	VAM vectors used for assimilation, thinning observations to 25 km	Assimilation of CYGNSS wind speed showed large improvements in the track, Vmax, and minimum sea level pressure. CYGNSS-derived vector winds helped the TC structure simulation to be more organized and symmetrical.
Impacts of Assimilating CYGNSS Satellite Ocean-Surface Wind on Prediction of Landfalling Hurricanes with the HWRF Model [92]	HWRF, 3DEnVAR	Real	Only wind speed was assimilated, thinning observations to 25 km	CYGNSS-retrieved ocean surface winds had positive impacts on the predicted track and intensity and also performed better in precipitation forecasts than ASCAT data.

Utilizing various methods to assimilate RO data leads to different impacts. The assimilation of bending angles performs better than refractivity and atmospheric profiles; it retains more information and needs more complicated observation operators. Assimilating refractivity or atmospheric profiles loses information inevitably due to the assumptions during the retrieval, but the operators used are concise. The assimilation of bending angles is significant for the global forecasts because the long propagation path can carry a cumulative effect, and the assimilation of refractivity or atmospheric profiles is more suitable for regional models and low layers. For the assimilation of GSNSS-R wind data, there are differences between assimilating GNSS-R wind speeds directly and VAM wind vectors. The TC structures are better described by VAM wind vectors. The assimilation involving wind directions makes the TC structure more organized than only assimilating wind speeds. The assimilation of VAM vectors also has a more positive impact on improving the accuracy of track and intensity forecasts. Wind data thinning also plays an important role in assimilation, and it helps reduce the risk of overfitting, although some information

is lost. We also found that by adjusting the observation errors, it might be possible to retain more GNSS-R wind speed data while improving the analyses and forecasts.

RO data assimilation is evolving towards multivariable and hybrid methods. However, challenges remain: different operators adapt to different atmospheric layers, adding complexity to models, and are bound to lose a certain amount of information. Moreover, in advanced bending angle assimilation, the nonlinearity of the cost function causes some optimization problems. GNSS-R data assimilation is a relatively new approach in TC forecasting. Aside from assimilating the wind speed, we can consider assimilating more raw data, such as DDM and NBRCS, to reduce observation errors for TC intensity forecasts, which requires the creation of more complex observation operators. Moreover, the research and analysis of GNSS-R observation errors have not been extensively studied, and further research in this area is needed.

6. Conclusions and Future Prospects

GNSS RO and GNSS-R technologies, with their unique advantages, effectively supplement the spatial and temporal limitations of traditional observation methods, particularly in the marine domain. Consequently, GNSS RS data have significantly improved the forecasting of typhoons. This article mainly reviews the assimilation applications of occultation and reflectometry observations in typhoon forecasting.

The article briefly introduces the principles of RO and GNSS-R, existing satellite missions, and their advantages, such as global coverage, high precision, and all-weather capability. It discusses the benefits that GNSS remote sensing data bring to typhoon forecasting. In the realm of TC monitoring, RO is one of the solutions to the longstanding issue of forecast errors. Assimilating RO data has significantly enhanced the predictions of TC intensity and trajectory, with data from below 6 km and the UTLS region aiding this improvement. At the early stages of a TC, data below 6 km are crucial due to RO's high vertical resolution, and UTLS data impact forecasts over three days or more. Additionally, the analysis of simulated TC vertical structures has reconstructed critical structures, especially the eye, eyewall, and rainbands, because RO data provide more accurate initial fields of moisture and temperature. The assimilation of RO in regions with high gradients of moisture and temperature remains challenging. However, the new method of a non-local excess phase operator has somewhat resolved this issue, further improving TC predictions. With denser RO data, TCs can be predicted more accurately.

GNSS-R in the field of TC detection mainly focuses on wind speed observations. Assimilating GNSS-R data has shown effectiveness in forecasting TC intensity and trajectory. The assimilation of CYGNSS wind data is more effective in improving path predictions, offering greater potential in representing vortex structures compared to conventional data assimilation and also aids in medium-range path forecasting. Ideally, the corresponding hurricane forecasts are improved within a 1-day timeframe, reducing errors in 0–48 h hurricane intensity predictions. The assimilation of VAM-CYGNSS vector winds can reduce MSW errors by 1–2.5 m/s and MSLP errors by 2–5 hPa. Statistical results of CYGNSS data assimilation are comparable to ASCAT, with reduced bias and root mean square errors. Currently, we hardly pay attention to the ocean surface wind speed error settings, but the error settings are important in the assimilation. In addition, there's nearly no study considering the correlation of ocean surface wind speed errors in data assimilation [14,95]. There is a potential that VAM is a good method to add directions for wind, but it has not been demonstrated in operational use. In this review article, most studies only evaluate the assimilation impact for one TC case, and researchers are encouraged to explore multiple TC scenarios for which results are more significant for operational use.

Finally, to serve TC forecasts better, the potential of RO and GNSS-R has been explored. People can develop methods for assimilating RO data by incorporating not only atmospheric physical variables and refractivity but also bending angles, thereby reducing errors while exploring new assimilation techniques. Additionally, more advanced RO technologies, such as polarized occultation, could be developed, which would enhance precipitation forecasts and provide better observations of TC structures. Regarding GNSS-R, currently, most studies only assimilate the GNSS-R ocean surface wind. Efforts can be made to assimilate GNSS-R NBRCS or even DDM [96,97] to capture more information from the lower-level observation. This method needs a more complex observation operator with its tangent linear operator, and we should supply the information, including satellite geometry, GNSS transmitting power, and receiver antenna parameters, which can usually be obtained from the GNSS-R Level 1 product. Furthermore, we can conduct the joint assimilation of RO and GNSS-R data, especially using data from GNSS-RO/R integrated missions, like the FY-3 series, where these two types of data complement each other, providing the potential to obtain more comprehensive forecasts of the TC intensity, trajectory, structure, and precipitation.

Author Contributions: Conceptualization, W.B. and F.H.; writing—original draft preparation, W.B., G.W. and F.H.; data curation, G.T., P.H., C.Y. and X.M.; resources, W.B., G.W., Y.S. and F.H.; funding acquisition, Y.S., Q.D., J.X., X.W. and R.W. All authors have read and agreed to the published version of the manuscript.

Funding: This research was funded by the Youth Cross Team Scientific Research Project of the Chinese Academy of Sciences grant number JCTD-2021-10, the National Natural Science Foundation of China grant number 42074042, and the Young Elite Scientist Sponsorship Program by CAST grant number 2023QNR001.

Data Availability Statement: No new data were created or analyzed in this study.

Conflicts of Interest: The authors declare no conflicts of interest.

References

1. Sobel, A.H.; Wing, A.A.; Camargo, S.J.; Patricola, C.M.; Vecchi, G.A.; Lee, C.Y.; Tippett, M.K. Tropical Cyclone Frequency. *Earth's Future* **2021**, *9*, e2021EF002275. [CrossRef]
2. Haupt, S.E.; Cowie, J.; Linden, S.; McCandless, T.; Kosovic, B.; Alessandrini, S. Machine Learning for Applied Weather Prediction. In Proceedings of the 2018 IEEE 14th International Conference on e-Science (e-Science), Amsterdam, The Netherlands, 29 October–1 November 2018; pp. 276–277.
3. Sura, P.; Cossuth, J.H.; Hart, R.E.; Fuelberg, H.E.; Halperin, D.J.; Pasch, R.J. An Evaluation of Tropical Cyclone Genesis Forecasts from Global Numerical Models. *Weather Forecast.* **2013**, *28*, 1423–1445. [CrossRef]
4. Halperin, D.J.; Penny, A.B.; Hart, R.E. A Comparison of Tropical Cyclone Genesis Forecast Verification from Three Global Forecast System (GFS) Operational Configurations. *Weather Forecast.* **2020**, *35*, 1801–1815. [CrossRef]
5. Halperin, D.J.; Fuelberg, H.E.; Hart, R.E.; Cossuth, J.H. Verification of Tropical Cyclone Genesis Forecasts from Global Numerical Models: Comparisons between the North Atlantic and Eastern North Pacific Basins. *Weather Forecast.* **2016**, *31*, 947–955. [CrossRef]
6. Wei, W.A.N.; Xiuwan, C.; Xuefeng, P.; Weihua, B.A.I.; Junming, X.I.A.; Hong, L.; Xuemin, Z.; Pan, X.; Ting, Y.; Yunchang, C.A.O.; et al. Overview and outlook of GNSS remote sensing technology and applications. *Natl. Remote Sens. Bull.* **2016**, *20*, 858–874. [CrossRef]
7. Jin, S.; Camps, A.; Jia, Y.; Wang, F.; Martin-Neira, M.; Huang, F.; Yan, Q.; Zhang, S.; Li, Z.; Edokossi, K.; et al. Remote sensing and its applications using GNSS reflected signals: Advances and prospects. *Satell. Navig.* **2024**, *5*, 19. [CrossRef]
8. Yu, X.; Xie, F.; Ao, C.O. Evaluating the lower-tropospheric COSMIC GPS radio occultation sounding quality over the Arctic. *Atmos. Meas. Tech.* **2018**, *11*, 2051–2066. [CrossRef]
9. Tournigand, P.-Y.; Cigala, V.; Prata, A.J.; Steiner, A.K.; Kirchengast, G.; Brenot, H.; Clarisse, L.; Biondi, R. The 2015 Calbuco Volcanic Cloud Detection Using GNSS Radio Occultation and Satellite Lidar. In Proceedings of the IGARSS 2020—2020 IEEE International Geoscience and Remote Sensing Symposium, Waikoloa, HI, USA, 26 September–2 October 2020; pp. 6834–6837.
10. Scherllin-Pirscher, B.; Steiner, A.K.; Kirchengast, G.; Schwärz, M.; Leroy, S.S. The power of vertical geolocation of atmospheric profiles from GNSS radio occultation. *J. Geophys. Res. Atmos.* **2017**, *122*, 1595–1616. [CrossRef]

11. Frehlich, R. Adaptive data assimilation including the effect of spatial variations in observation error. *Q. J. R. Meteorol. Soc.* **2007**, *132*, 1225–1257. [CrossRef]
12. Blackwell, W.J.; Bishop, R.; Cahoy, K.; Cohen, B.; Crail, C.; Cucurull, L.; Dave, P.; DiLiberto, M.; Erickson, N.; Fish, C.; et al. Radiometer Calibration Using Colocated GPS Radio Occultation Measurements. *IEEE Trans. Geosci. Remote Sens.* **2014**, *52*, 6423–6433. [CrossRef]
13. Rodriguez-Alvarez, N.; Munoz-Martin, J.F.; Morris, M. Latest Advances in the Global Navigation Satellite System—Reflectometry (GNSS-R) Field. *Remote Sens.* **2023**, *15*, 2157. [CrossRef]
14. Powell, C.E.; Ruf, C.S.; McKague, D.S.; Wang, T.; Russel, A. An Instrument Error Correlation Model for Global Navigation Satellite System Reflectometry. *Remote Sens.* **2024**, *16*, 742. [CrossRef]
15. Durazo, J.A.; Kostelich, E.J.; Mahalov, A. Local ensemble transform Kalman filter for ionospheric data assimilation: Observation influence analysis during a geomagnetic storm event. *J. Geophys. Res. Space Phys.* **2017**, *122*, 9652–9669. [CrossRef]
16. Vannitsem, S.; Carrassi, A. Accounting for Model Error in Variational Data Assimilation: A Deterministic Formulation. *Mon. Weather Rev.* **2010**, *138*, 3369–3386. [CrossRef]
17. Lasota, E.; Steiner, A.K.; Kirchengast, G.; Biondi, R. Tropical cyclones vertical structure from GNSS radio occultation: An archive covering the period 2001–2018. *Earth Syst. Sci. Data* **2020**, *12*, 2679–2693. [CrossRef]
18. Zavorotny, V.U.; Voronovich, A.G. Scattering of GPS signals from the ocean with wind remote sensing application. *IEEE Trans. Geosci. Remote Sens.* **2000**, *38*, 951–964. [CrossRef]
19. Ruf, C.S.; Balasubramaniam, R. Development of the CYGNSS Geophysical Model Function for Wind Speed. *IEEE J. Sel. Top. Appl. Earth Obs. Remote Sens.* **2019**, *12*, 66–77. [CrossRef]
20. Clarizia, M.P.; Ruf, C.S.; Jales, P.; Gommenginger, C. Spaceborne GNSS-R Minimum Variance Wind Speed Estimator. *IEEE Trans. Geosci. Remote Sens.* **2014**, *52*, 6829–6843. [CrossRef]
21. Clarizia, M.P.; Ruf, C.S. Wind Speed Retrieval Algorithm for the Cyclone Global Navigation Satellite System (CYGNSS) Mission. *IEEE Trans. Geosci. Remote Sens.* **2016**, *54*, 4419–4432. [CrossRef]
22. Alsweiss, S.; Jelenak, Z.; Chang, P. All-Weather Geophysical Model Function for Wind Speed Retrievals from AMSR2. In Proceedings of the IGARSS 2022—2022 IEEE International Geoscience and Remote Sensing Symposium, Kuala Lumpur, Malaysia, 17–22 July 2022; pp. 6915–6918.
23. Zhang, Y.; Wang, Y.; Zhang, J.; Liu, Y. Reanalysis of the Tilt MTFs Based on the C-Band Empirical Geophysical Model Function. *IEEE Geosci. Remote Sens. Lett.* **2021**, *18*, 1500–1504. [CrossRef]
24. Lin, W.; Portabella, M.; Foti, G.; Stoffelen, A.; Gommenginger, C.; He, Y. Toward the Generation of a Wind Geophysical Model Function for Spaceborne GNSS-R. *IEEE Trans. Geosci. Remote Sens.* **2019**, *57*, 655–666. [CrossRef]
25. Sun, Y.; Huang, F.; Xia, J.; Yin, C.; Bai, W.; Du, Q.; Wang, X.; Cai, Y.; Li, W.; Yang, G.; et al. GNOS-II on Fengyun-3 Satellite Series: Exploration of Multi-GNSS Reflection Signals for Operational Applications. *Remote Sens.* **2023**, *15*, 5756. [CrossRef]
26. Berman, A.L.; Ramos, R. Pioneer Venus Occultation Radio Science Data Generation. *IEEE Trans. Geosci. Remote Sens.* **1980**, *GE-18*, 11–14. [CrossRef]
27. English, S.J.; Bauer, P.; Healy, S.B.; Harnisch, F. Scaling of GNSS Radio Occultation Impact with Observation Number Using an Ensemble of Data Assimilations. *Mon. Weather Rev.* **2013**, *141*, 4395–4413. [CrossRef]
28. Ware, R.; Rocken, C.; Solheim, F.; Exner, M.; Schreiner, W.; Anthes, R.; Feng, D.; Herman, B.; Gorbunov, M.; Sokolovskiy, S.; et al. GPS Sounding of the Atmosphere from Low Earth Orbit: Preliminary Results. *Bull. Am. Meteorol. Soc.* **1996**, *77*, 19–40. [CrossRef]
29. Kuo, Y.H.; Zou, X.; Chen, S.J.; Huang, W.; Guo, Y.R.; Anthes, R.A.; Exner, M.; Hunt, D.; Rocken, C.; Sokolovskiy, S. A GPS/MET Sounding through an Intense Upper-Level Front. *Bull. Am. Meteorol. Soc.* **1998**, *79*, 617–626. [CrossRef]
30. Kim, H.R.; von Frese, R.R.B.; Kim, J.W.; Taylor, P.T.; Neubert, T. Ørsted verifies regional magnetic anomalies of the Antarctic lithosphere. *Geophys. Res. Lett.* **2002**, *29*, ORS-3. [CrossRef]
31. Yunck, T.P.; Liu, C.-H.; Ware, R. A History of GPS Sounding. *Terr. Atmos. Ocean. Sci.* **2000**, *11*, 1–20. [CrossRef]
32. Reigber, C.; Balmino, G.; Schwintzer, P.; Biancale, R.; Bode, A.; Lemoine, J.M.; König, R.; Loyer, S.; Neumayer, H.; Marty, J.C.; et al. Global Gravity Field Recovery Using Solely GPS Tracking and Accelerometer Data from Champ. *Space Sci. Rev.* **2003**, *108*, 55–66. [CrossRef]
33. Colomb, R.; Alonso, C.; Nollmann, I. SAC-C mission and the international am constellation for earth observation. *Acta Astronaut.* **2003**, *52*, 995–1005. [CrossRef]
34. Anthes, R.A. Exploring Earth's atmosphere with radio occultation: Contributions to weather, climate and space weather. *Atmos. Meas. Tech.* **2011**, *4*, 1077–1103. [CrossRef]
35. Norman, R.J.; Dyson, P.L.; Yizengaw, E.; Le Marshall, J.; Wang, C.-S.; Carter, B.A.; Wen, D.; Zhang, K. Radio Occultation Measurements From the Australian Microsatellite FedSat. *IEEE Trans. Geosci. Remote Sens.* **2012**, *50*, 4832–4839. [CrossRef]
36. Kalmus, P.; Ao, C.O.; Wang, K.-N.; Manzi, M.P.; Teixeira, J. A high-resolution planetary boundary layer height seasonal climatology from GNSS radio occultations. *Remote Sens. Environ.* **2022**, *276*, 113037. [CrossRef]

37. Wickert, J.; Michalak, G.; Schmidt, T.; Beyerle, G.; Cheng, C.-Z.; Healy, S.B.; Heise, S.; Huang, C.-Y.; Jakowski, N.; Köhler, W.; et al. GPS Radio Occultation: Results from CHAMP, GRACE and FORMOSAT-3/COSMIC. *Terr. Atmos. Ocean. Sci.* **2009**, *20*, 35–50. [CrossRef]
38. Hao, N.; Koukouli, M.E.; Inness, A.; Valks, P.; Loyola, D.G.; Zimmer, W.; Balis, D.S.; Zyrichidou, I.; Van Roozendael, M.; Lerot, C.; et al. GOME-2 total ozone columns from MetOp-A/MetOp-B and assimilation in the MACC system. *Atmos. Meas. Tech.* **2014**, *7*, 2937–2951. [CrossRef]
39. Montenbruck, O.; Andres, Y.; Bock, H.; van Helleputte, T.; van den Ijssel, J.; Loiselet, M.; Marquardt, C.; Silvestrin, P.; Visser, P.; Yoon, Y. Tracking and orbit determination performance of the GRAS instrument on MetOp-A. *GPS Solut.* **2008**, *12*, 289–299. [CrossRef]
40. Cardellach, E.; Tomas, S.; Oliveras, S.; Padulles, R.; Rius, A.; de la Torre-Juarez, M.; Turk, F.J.; Ao, C.O.; Kursinski, E.R.; Schreiner, B.; et al. Sensitivity of PAZ LEO Polarimetric GNSS Radio-Occultation Experiment to Precipitation Events. *IEEE Trans. Geosci. Remote Sens.* **2015**, *53*, 190–206. [CrossRef]
41. Martin-Neira, M.; Caparrini, M.; Font-Rossello, J.; Lannelongue, S.; Vallmitjana, C.S. The PARIS concept: An experimental demonstration of sea surface altimetry using GPS reflected signals. *IEEE Trans. Geosci. Remote Sens.* **2001**, *39*, 142–150. [CrossRef]
42. Kursinski, E.R.; Hajj, G.A.; Schofield, J.T.; Linfield, R.P.; Hardy, K.R. Observing Earth's atmosphere with radio occultation measurements using the Global Positioning System. *J. Geophys. Res. Atmos.* **1997**, *102*, 23429–23465. [CrossRef]
43. Foti, G.; Gommenginger, C.; Jales, P.; Unwin, M.; Shaw, A.; Robertson, C.; Roselló, J. Spaceborne GNSS reflectometry for ocean winds: First results from the UK TechDemoSat-1 mission. *Geophys. Res. Lett.* **2015**, *42*, 5435–5441. [CrossRef]
44. Said, F.; Katzberg, S.J.; Soisuvarn, S. Retrieving Hurricane Maximum Winds Using Simulated CYGNSS Power-Versus-Delay Waveforms. *IEEE J. Sel. Top. Appl. Earth Obs. Remote Sens.* **2017**, *10*, 3799–3809. [CrossRef]
45. Ho, S.-p.; Zhou, X.; Shao, X.; Chen, Y.; Jing, X.; Miller, W. Using the Commercial GNSS RO Spire Data in the Neutral Atmosphere for Climate and Weather Prediction Studies. *Remote Sens.* **2023**, *15*, 4836. [CrossRef]
46. Unwin, M.J.; Pierdicca, N.; Cardellach, E.; Rautiainen, K.; Foti, G.; Blunt, P.; Guerriero, L.; Santi, E.; Tossaint, M. An Introduction to the HydroGNSS GNSS Reflectometry Remote Sensing Mission. *IEEE J. Sel. Top. Appl. Earth Obs. Remote Sens.* **2021**, *14*, 6987–6999. [CrossRef]
47. Bai, W.H.; Sun, Y.Q.; Du, Q.F.; Yang, G.L.; Yang, Z.D.; Zhang, P.; Bi, Y.M.; Wang, X.Y.; Cheng, C.; Han, Y. An introduction to the FY3 GNOS instrument and mountain-top tests. *Atmos. Meas. Tech.* **2014**, *7*, 1817–1823. [CrossRef]
48. Wei, J.; Li, Y.; Zhang, K.; Liao, M.; Bai, W.; Liu, C.; Liu, Y.; Wang, X. An Evaluation of Fengyun-3C Radio Occultation Atmospheric Profiles Over 2015–2018. *Remote Sens.* **2020**, *12*, 2116. [CrossRef]
49. Bai, W.; Wang, G.; Sun, Y.; Shi, J.; Yang, G.; Meng, X.; Wang, D.; Du, Q.; Wang, X.; Xia, J.; et al. Application of the Fengyun 3 C GNSS occultation sounder for assessing the global ionospheric response to a magnetic storm event. *Atmos. Meas. Tech.* **2019**, *12*, 1483–1493. [CrossRef]
50. Qiu, T.; Wang, X.; Sun, Y.; Li, F.; Wang, Z.; Xia, J.; Du, Q.; Bai, W.; Cai, Y.; Wang, D.; et al. An Innovative Signal Processing Scheme for Spaceborne Integrated GNSS Remote Sensors. *Remote Sens.* **2023**, *15*, 745. [CrossRef]
51. Huang, F.; Sun, Y.; Xia, J.; Yin, C.; Bai, W.; Du, Q.; Zhai, X.; Yang, G.; Chen, L.; Lu, W.; et al. Progress on the GNSS-R Product from Fengyun-3 Missions. In Proceedings of the IGARSS 2024—2024 IEEE International Geoscience and Remote Sensing Symposium, Athens, Greece, 7–12 July 2024; pp. 6717–6720.
52. Zheng, W.; Hsu, H.; Zhong, M.; Yun, M. China's first-phase Mars Exploration Program: Yinghuo-1 orbiter. *Planet. Space Sci.* **2013**, *86*, 155–159. [CrossRef]
53. Jing, C.; Li, W.; Wan, W.; Lu, F.; Niu, X.; Chen, X.; Rius, A.; Cardellach, E.; Ribó, S.; Liu, B.; et al. A review of the BuFeng-1 GNSS-R mission: Calibration and validation results of sea surface and land surface. *Geo-Spat. Inf. Sci.* **2024**, *27*, 638–652. [CrossRef]
54. Agency, X.N. China's Commercial Rocket CERES-1 Y5 Launches 5 Satellites. Available online: https://english.www.gov.cn/news/photos/202301/09/content_WS63bbf654c6d0a757729e5498.html (accessed on 5 January 2023).
55. Healy, S.B.; Thépaut, J.N. Assimilation experiments with CHAMP GPS radio occultation measurements. *Q. J. R. Meteorol. Soc.* **2006**, *132*, 605–623. [CrossRef]
56. Vergados, P.; Mannucci, A.J.; Su, H. A validation study for GPS radio occultation data with moist thermodynamic structure of tropical cyclones. *J. Geophys. Res. Atmos.* **2013**, *118*, 9401–9413. [CrossRef]
57. Ho, S.-p.; Pedatella, N.; Foelsche, U.; Healy, S.; Weiss, J.-P.; Ullman, R. Using Radio Occultation Data for Atmospheric Numerical Weather Prediction, Climate Sciences, and Ionospheric Studies and Initial Results from COSMIC-2, Commercial RO Data, and Recent RO Missions. *Bull. Am. Meteorol. Soc.* **2022**, *103*, E2506–E2512. [CrossRef]
58. Biondi, R.; Steiner, A.K.; Kirchengast, G.; Rieckh, T. Characterization of thermal structure and conditions for overshooting of tropical and extratropical cyclones with GPS radio occultation. *Atmos. Chem. Phys.* **2015**, *15*, 5181–5193. [CrossRef]
59. Biondi, R.; Neubert, T. Bending Angle and Temperature Climatologies from Global Positioning System Radio Occultations. *Dataset Pap. Geosci.* **2013**, *2013*, 795749. [CrossRef]

60. Yang, S.; Zou, X.; Ray, P.S. Comparison of TC Temperature and Water Vapor Climatologies between the Atlantic and Pacific Oceans from GPS RO Observations. *J. Clim.* **2018**, *31*, 8557–8571. [CrossRef]
61. Kuo, Y.-H.; Anderson, J.; Liu, H. Improved Analyses and Forecasts of Hurricane Ernesto's Genesis Using Radio Occultation Data in an Ensemble Filter Assimilation System. *Mon. Weather Rev.* **2012**, *140*, 151–166. [CrossRef]
62. Ma, L.; Jiang, Z.; Shen, T. The Improved Genetic Algorithm and the Application of It in MM5 Model of Four-Dimensional Variational Data Assimilation System. In Proceedings of the 2009 First International Conference on Information Science and Engineering, Nanjing, China, 26–28 December 2009; pp. 5218–5221.
63. Yueqi, H.; Zhong, Z.; Zhuhui, W.; Yunfeng, W.; Xiaoping, C. An ensemble-based three-dimensional variational data assimilation scheme. In Proceedings of the 2011 International Conference on Multimedia Technology, Hangzhou, China, 26–28 July 2011; pp. 1961–1964.
64. Chen, S.-Y.; Nguyen, T.-C.; Huang, C.-Y. Impact of Radio Occultation Data on the Prediction of Typhoon Haishen (2020) with WRFDA Hybrid Assimilation. *Atmosphere* **2021**, *12*, 1397. [CrossRef]
65. Burrows, C.P.; Healy, S.B.; Culverwell, I.D. Improving the bias characteristics of the ROPP refractivity and bending angle operators. *Atmos. Meas. Tech.* **2014**, *7*, 3445–3458. [CrossRef]
66. Liu, H.; Kuo, Y.-H.; Sokolovskiy, S.; Zou, X.; Zeng, Z.; Hsiao, L.-F.; Ruston, B.C. A Quality Control Procedure Based on Bending Angle Measurement Uncertainty for Radio Occultation Data Assimilation in the Tropical Lower Troposphere. *J. Atmos. Ocean. Technol.* **2018**, *35*, 2117–2131. [CrossRef]
67. Chen, S.-Y.; Huang, C.-Y.; Kuo, Y.-H.; Guo, Y.-R.; Shiau, S. Assimilation of GPS Refractivity from FORMOSAT-3/COSMIC Using a Nonlocal Operator with WRF 3DVAR and Its Impact on the Prediction of a Typhoon Event. *Terr. Atmos. Ocean. Sci.* **2009**, *20*, 133–154. [CrossRef]
68. Chen, S.-Y.; Kuo, Y.-H.; Huang, C.-Y. The Impact of GPS RO Data on the Prediction of Tropical Cyclogenesis Using a Nonlocal Observation Operator: An Initial Assessment. *Mon. Weather Rev.* **2020**, *148*, 2701–2717. [CrossRef]
69. Cucurull, L.; Derber, J.C.; Purser, R.J. A bending angle forward operator for global positioning system radio occultation measurements. *J. Geophys. Res. Atmos.* **2013**, *118*, 14–28. [CrossRef]
70. Gilpin, S.; Anthes, R.; Sokolovskiy, S. Sensitivity of Forward-Modeled Bending Angles to Vertical Interpolation of Refractivity for Radio Occultation Data Assimilation. *Mon. Weather Rev.* **2019**, *147*, 269–289. [CrossRef]
71. Huang, C.-Y.; Chen, S.-Y.; Rao Anisetty, S.K.A.V.P.; Yang, S.-C.; Hsiao, L.-F. An Impact Study of GPS Radio Occultation Observations on Frontal Rainfall Prediction with a Local Bending Angle Operator. *Weather Forecast.* **2016**, *31*, 129–150. [CrossRef]
72. Wee, T.K.; Kuo, Y.H.; Lee, D.K. Development of a curved ray tracing method for modeling of phase paths from GPS radio occultation: A two-dimensional study. *J. Geophys. Res. Atmos.* **2010**, *115*, D24119. [CrossRef]
73. Poli, P. Effects of horizontal gradients on GPS radio occultation observation operators. II: A Fast Atmospheric Refractivity Gradient Operator (FARGO). *Q. J. R. Meteorol. Soc.* **2006**, *130*, 2807–2825. [CrossRef]
74. Teng, H.F.; Kuo, Y.H.; Done, J.M. Potential Impacts of Radio Occultation Data Assimilation on Forecast Skill of Tropical Cyclone Formation in the Western North Pacific. *Geophys. Res. Lett.* **2023**, *50*, e2021GL096750. [CrossRef]
75. Schwarz, J.; Kirchengast, G.; Schwaerz, M. Integrating uncertainty propagation in GNSS radio occultation retrieval: From excess phase to atmospheric bending angle profiles. *Atmos. Meas. Tech.* **2018**, *11*, 2601–2631. [CrossRef]
76. Miller, W.J.; Chen, Y.; Ho, S.-P.; Shao, X. Evaluating the Impacts of COSMIC-2 GNSS RO Bending Angle Assimilation on Atlantic Hurricane Forecasts Using the HWRF Model. *Mon. Weather Rev.* **2023**, *151*, 1821–1847. [CrossRef]
77. Peevey, T.R.; Atlas, R.; Hoffman, R.N.; Casey, S.P.F.; Cucurull, L.; Kren, A.C.; Mueller, M.J. Impact of Refractivity Profiles from a Proposed GNSS-RO Constellation on Tropical Cyclone Forecasts in a Global Modeling System. *Mon. Weather Rev.* **2020**, *148*, 3037–3057. [CrossRef]
78. Kunii, M.; Seko, H.; Ueno, M.; Shoji, Y.; Tsuda, T. Impact of Assimilation of GPS Radio Occultation Refractivity on the Forecast of Typhoon Usagi in 2007. *J. Meteorol. Soc. Japan. Ser. II* **2012**, *90*, 255–273. [CrossRef]
79. Chen, S.-Y.; Shih, C.-P.; Huang, C.-Y.; Teng, W.-H. An Impact Study of GNSS RO Data on the Prediction of Typhoon Nepartak (2016) Using a Multiresolution Global Model with 3D-Hybrid Data Assimilation. *Weather Forecast.* **2021**, *36*, 957–977. [CrossRef]
80. Cucurull, L.; Mueller, M.J. An Analysis of Alternatives for the COSMIC-2 Constellation in the Context of Global Observing System Simulation Experiments. *Weather Forecast.* **2020**, *35*, 51–66. [CrossRef]
81. Ruston, B.; Healy, S. Forecast Impact of FORMOSAT-7/COSMIC-2 GNSS Radio Occultation Measurements. *Atmos. Sci. Lett.* **2020**, *22*, e1019. [CrossRef]
82. Cucurull, L. Recent Impact of COSMIC-2 with Improved Radio Occultation Data Assimilation Algorithms. *Weather Forecast.* **2023**, *38*, 1829–1847. [CrossRef]
83. Li, C.; Huang, W.; Gleason, S. Dual Antenna Space-Based GNSS-R Ocean Surface Mapping: Oil Slick and Tropical Cyclone Sensing. *IEEE J. Sel. Top. Appl. Earth Obs. Remote Sens.* **2015**, *8*, 425–435. [CrossRef]
84. Mayers, D.R.; Ruf, C.S.; Warnock, A.M. CYGNSS Storm-Centric Tropical Cyclone Gridded Wind Speed Product. *J. Appl. Meteorol. Climatol.* **2023**, *62*, 329–339. [CrossRef]

85. Warnock, A.M.; Ruf, C.S.; Russel, A.; Al-Khaldi, M.M.; Balasubramaniam, R. CYGNSS Level 3 Merged Wind Speed Data Product for Storm Force and Surrounding Environmental Winds. *IEEE J. Sel. Top. Appl. Earth Obs. Remote Sens.* **2024**, *17*, 6189–6200. [CrossRef]
86. Leidner, S.M.; Annane, B.; McNoldy, B.; Hoffman, R.; Atlas, R. Variational Analysis of Simulated Ocean Surface Winds from the Cyclone Global Navigation Satellite System (CYGNSS) and Evaluation Using a Regional OSSE. *J. Atmos. Ocean. Technol.* **2018**, *35*, 1571–1584. [CrossRef]
87. Majumdar, S.J.; Atlas, R.; Hoffman, R.; Leidner, S.M.; McNoldy, B.; Annane, B. A Study of the HWRF Analysis and Forecast Impact of Realistically Simulated CYGNSS Observations Assimilated as Scalar Wind Speeds and as VAM Wind Vectors. *Mon. Weather Rev.* **2018**, *146*, 2221–2236. [CrossRef]
88. Zhang, S.; Pu, Z.; Posselt, D.J.; Atlas, R. Impact of CYGNSS Ocean Surface Wind Speeds on Numerical Simulations of a Hurricane in Observing System Simulation Experiments. *J. Atmos. Ocean. Technol.* **2017**, *34*, 375–383. [CrossRef]
89. McNoldy, B.; Annane, B.; Majumdar, S.; Delgado, J.; Bucci, L.; Atlas, R. Impact of Assimilating CYGNSS Data on Tropical Cyclone Analyses and Forecasts in a Regional OSSE Framework. *Mar. Technol. Soc. J.* **2017**, *51*, 7–15. [CrossRef]
90. Li, X.; Mecikalski, J.R.; Lang, T.J. A Study on Assimilation of CYGNSS Wind Speed Data for Tropical Convection during 2018 January MJO. *Remote Sens.* **2020**, *12*, 1243. [CrossRef]
91. Mueller, M.J.; Annane, B.; Leidner, S.M.; Cucurull, L. Impact of CYGNSS-Derived Winds on Tropical Cyclone Forecasts in a Global and Regional Model. *Mon. Weather Rev.* **2021**, *149*, 3433–3447. [CrossRef]
92. Pu, Z.; Wang, Y.; Li, X.; Ruf, C.; Bi, L.; Mehra, A. Impacts of Assimilating CYGNSS Satellite Ocean-Surface Wind on Prediction of Landfalling Hurricanes with the HWRF Model. *Remote Sens.* **2022**, *14*, 2118. [CrossRef]
93. Yang, S.C.; Chen, S.H.; Chang, C.C. Understanding the impact of assimilating FORMOSAT-7/COSMIC-2 radio occultation refractivity on tropical cyclone genesis: Observing system simulation experiments using Hurricane Gordon (2006) as a case study. *Q. J. R. Meteorol. Soc.* **2023**, *149*, 1293–1318. [CrossRef]
94. Chien, T.-Y.; Chen, S.-Y.; Huang, C.-Y.; Shih, C.-P.; Schwartz, C.S.; Liu, Z.; Bresch, J.; Lin, J.-Y. Impacts of Radio Occultation Data on Typhoon Forecasts as Explored by the Global MPAS-GSI System. *Atmosphere* **2022**, *13*, 1353. [CrossRef]
95. Powell, C.E.; Ruf, C.S.; Gleason, S.; Rafkin, S.C.R. Sampled Together: Assessing the Value of Simultaneous Collocated Measurements for Optimal Satellite Configurations. *Bull. Am. Meteorol. Soc.* **2024**, *105*, E285–E296. [CrossRef]
96. Huang, F.; Garrison, J.L.; Mark Leidner, S.; Grieco, G.; Stoffelen, A.; Annane, B.; Hoffman, R.N. Assimilation of GNSS reflectometry delay-Doppler maps with a two-dimensional variational analysis of global ocean surface winds. *Q. J. R. Meteorol. Soc.* **2021**, *147*, 2469–2489. [CrossRef]
97. Huang, F.; Garrison, J.L.; Leidner, S.M.; Annane, B.; Hoffman, R.N.; Grieco, G.; Stoffelen, A. A Forward Model for Data Assimilation of GNSS Ocean Reflectometry Delay-Doppler Maps. *IEEE Trans. Geosci. Remote Sens.* **2021**, *59*, 2643–2656. [CrossRef]

Disclaimer/Publisher's Note: The statements, opinions and data contained in all publications are solely those of the individual author(s) and contributor(s) and not of MDPI and/or the editor(s). MDPI and/or the editor(s) disclaim responsibility for any injury to people or property resulting from any ideas, methods, instructions or products referred to in the content.